

# Climate Process Team on Internal-Wave Driven Ocean Mixing

Jennifer A. MacKinnon \*

*Scripps Institution of Oceanography, La Jolla USA*

Matthew H. Alford

*Scripps Institution of Oceanography, La Jolla USA*

Joseph K. Ansong

*Department of Earth and Environmental Sciences, University of Michigan, Ann Arbor USA*

Brian K. Arbic

*Department of Earth and Environmental Sciences, University of Michigan, Ann Arbor USA*

Andrew Barna

*Scripps Institution of Oceanography, La Jolla USA*

Bruce P. Briegleb

*National Center for Atmospheric Research, Boulder, CO USA*

Frank O. Bryan

*National Center for Atmospheric Research, Boulder, CO USA*

Maarten C. Buijsman

*Division of Marine Science, University of Southern Mississippi, Stennis Space Center, USA*

Eric P. Chassignet

*Center for Ocean-Atmospheric Prediction Studies, Florida State University, Tallahassee, USA*

Gokhan Danabasoglu

*National Center for Atmospheric Research, Boulder, CO USA*

Steve Diggs

*Scripps Institution of Oceanography, La Jolla USA*

Stephen M. Griffies

*NOAA Geophysical Fluid Dynamics Laboratory, Princeton USA*

Robert W. Hallberg

*NOAA Geophysical Fluid Dynamics Laboratory, Princeton USA*

Steven R. Jayne

*Woods Hole Oceanographic Institution, Woods Hole, Massachusetts, USA*

Markus Jochum

*Niels Bohr Institute, Copenhagen, Denmark*

Jody M. Klymak

*University of Victoria, Canada*

Eric Kunze

*Northwest Research Associates, Seattle, WA*

William G. Large

37 *National Center for Atmospheric Research, Boulder, CO USA*

38 Sonya Legg

39 *Program in Atmospheric and Oceanic Sciences, Princeton University, Princeton, USA*

40 Benjamin Mater

41 *Program in Atmospheric and Oceanic Sciences, Princeton University, Princeton, USA*

42 Angelique V. Melet

43 *Program in Atmospheric and Oceanic Sciences, Princeton University, Princeton, USA*

44 *Mercator Ocean, Ramonville St Agne, France*

45 Lynne M. Merchant

46 *Scripps Institution of Oceanography, La Jolla USA*

47 Ruth Musgrave

48 *Massachusetts Institute of Technology, Cambridge, USA*

49 Jonathan D. Nash

50 *Oregon State University, Corvallis, OR, USA*

51 Nancy J. Norton

52 *National Center for Atmospheric Research, Boulder, CO USA*

53 Andrew Pickering

54 *Oregon State University, Corvallis, OR, USA*

55 Robert Pinkel

56 *Scripps Institution of Oceanography, La Jolla USA*

57 Kurt Polzin

58 *Woods Hole Oceanographic Institution, Woods Hole, Massachusetts, USA*

59 Harper L. Simmons

60 *University of Alaska Fairbanks, Fairbanks, Alaska USA*

61 Louis C. St. Laurent

62 *Woods Hole Oceanographic Institution, Woods Hole, Massachusetts, USA*

63 Oliver M. Sun

64 *Woods Hole Oceanographic Institution, Woods Hole, Massachusetts, USA*

65 David S. Trossman

66 *Goddard Earth Sciences Technology and Research, Greenbelt, Maryland, USA*

67 *Department of Earth and Planetary Sciences, Johns Hopkins University, Baltimore USA*

68 Amy F. Waterhouse

69 *Scripps Institution of Oceanography, La Jolla USA*

70 Caitlin B. Whalen

71 *Applied Physics Laboratory, University of Washington, Seattle, Washington, USA*

72 Zhongxiang Zhao

73 *Applied Physics Laboratory, University of Washington, Seattle, Washington, USA*



<sup>74</sup> \**Corresponding author address:* 9500 Gilman Drive, M/C 0213, La Jolla, CA 92093

<sup>75</sup> E-mail: [jmackinnon@ucsd.edu](mailto:jmackinnon@ucsd.edu)

## ABSTRACT

76 Diapycnal mixing plays a primary role in the thermodynamic balance of  
77 the ocean and, consequently, in oceanic heat and carbon uptake and stor-  
78 age. Though observed mixing rates are on average consistent with values  
79 required by inverse models, recent attention has focused on the dramatic spa-  
80 tial variability, spanning several orders of magnitude, of mixing rates in both  
81 the upper and deep ocean. Away from ocean boundaries, the spatio-temporal  
82 patterns of mixing are largely driven by the geography of generation, propa-  
83 gation and dissipation of internal waves, which supply much of the power for  
84 turbulent mixing. Over the last five years and under the auspices of US CLI-  
85 VAR, a NSF- and NOAA-supported Climate Process Team has been engaged  
86 in developing, implementing and testing dynamics-based parameterizations  
87 for internal-wave driven turbulent mixing in global ocean models. The work  
88 has primarily focused on turbulence 1) near sites of internal tide generation,  
89 2) in the upper ocean related to wind-generated near inertial motions, 3) due  
90 to internal lee waves generated by low-frequency mesoscale flows over topog-  
91 raphy, and 4) at ocean margins. Here we review recent progress, describe the  
92 tools developed, and discuss future directions.

# 93 1. Introduction

## 94 a. Context

95 Ocean turbulence influences the transport of heat, freshwater, dissolved gases such as CO<sub>2</sub>, pol-  
96 lutants and other tracers. It is central to understanding ocean energetics and reducing uncertainties  
97 in global circulation and simulations from climate models. The dissipation of turbulent energy in  
98 stratified water results in irreversible diapycnal (across density surfaces) mixing. Recent work has  
99 shown that the spatial and temporal inhomogeneity in diapycnal mixing may play a critical role in  
100 a variety of climate phenomena. Hence a quantitative understanding of the physics that drive the  
101 distribution of diapycnal mixing in the ocean interior is fundamental to understanding the ocean's  
102 role in climate.

103 Diapycnal mixing is very difficult to accurately parameterize in numerical ocean models for two  
104 reasons. The first one is due to the discrete representation of tracer advection in directions that  
105 are not perfectly aligned with isopycnals, which can result in numerically induced mixing from  
106 truncation errors that is larger than observed diapycnal mixing (Griffies et al. 2000; Ilıcak et al.  
107 2012). The second reason is related to the intermittency of turbulence, which is generated by com-  
108 plex and chaotic motions that span a large space-time range. Furthermore, this mixing is driven  
109 by a wide range of processes with distinct governing physics that create a rich global geography  
110 (see MacKinnon et al. (2013a) for a review). The difficulty is also related to the relatively sparse  
111 direct sampling of ocean mixing, whereby sophisticated ship-based measurements are generally  
112 required to accurately characterize ocean mixing processes. Nonetheless, we have sufficient evi-  
113 dence from theory, process models, laboratory experiments, and field measurements to conclude  
114 that away from ocean boundaries (atmosphere, ice, or the solid ocean bottom), diapycnal mixing is  
115 largely related to the *breaking of internal gravity waves*, which have a complex dynamical under-

pinning and associated geography. Consequently, in 2010, a Climate Process Team (CPT), funded by the National Science Foundation and the National Atmospheric and Oceanic Administration, was convened to consolidate knowledge on internal-wave-driven turbulent mixing in the ocean, develop new and more accurate parameterizations suitable for global ocean models, and consider the consequences for global circulation and climate. Here we report on the major findings and products from this CPT.

Ocean internal gravity waves propagate through the stratified interior of the ocean. They are generated by a variety of mechanisms, with the most important being tidal flow over topography, wind variations at the sea-surface, and flow of ocean currents and eddies over topography leading to lee-waves (see schematic in Figure 1). As waves propagate horizontally and vertically away from their generation sites, they interact with each other, producing an internal gravity wave continuum consisting of energy in many frequencies and wavenumbers. The waves with high vertical wavenumbers (small vertical scales) are more likely to break, leading to turbulent mixing. The distribution of diapycnal mixing therefore depends on the entire chain of processes shown in Figure 1.

#### *b. A brief history of vertical mixing parameterizations used by ocean models*

Ocean models often approximate diapycnal mixing processes through vertical Fickian diffusion, which takes the mathematical form

$$\text{Fickian diffusion} = \frac{\partial}{\partial z} \left( \kappa \frac{\partial \psi}{\partial z} \right), \quad (1)$$

where  $\psi$  is the tracer concentration,  $z$  is the geopotential vertical coordinate, and  $\kappa$  is the diapycnal diffusivity (dimensions of  $L^2 T^{-1}$ ). Through the 1990s, global models routinely used space-time constant vertical diffusivities. A notable exception was Bryan and Lewis (1979), who prescribed

137 a horizontally uniform diffusivity that increased with depth, reflecting the observed larger vertical  
138 mixing in the deep ocean and reduced mixing in the pycnocline. By the mid-1990s, ocean climate  
139 models began to separate diapycnal mixing into surface boundary layer and interior processes. In  
140 and near the surface boundary layer, mixing is controlled by a balance between buoyancy input  
141 (e.g., heat and freshwater fluxes) and mechanical forcing (e.g., wind) that establish the surface  
142 boundary layer and fluxes through it. Climate models of this era used boundary layer schemes  
143 such as Gaspar et al. (1990) and Large et al. (1994). In the stably stratified ocean interior, both  
144 shear-driven mixing (Pacanowski and Philander 1981; Large et al. 1994) and double-diffusive  
145 processes (Large et al. 1994) were parameterized. Gravitational instabilities giving rise to vertical  
146 convection were accounted for through a large vertical diffusivity (Large et al. 1994; Klinger et al.  
147 1996) or a convective adjustment scheme (Rahmstorf 1993).

148 In the deep ocean, a prognostic parameterization for internal tide-driven mixing was introduced  
149 by St. Laurent et al. (2002), who combined an estimate of internal tide generation over rough to-  
150 pography with an empirical vertical decay scale for the enhanced turbulence (see Section 3). State-  
151 of-the-art ocean climate simulations prior to the CPT, as represented by the Geophysical Fluid  
152 Dynamics Laboratory (GFDL) and National Center for Atmospheric Research (NCAR) CMIP5  
153 simulations (Dunne et al. 2012; Danabasoglu et al. 2012), included a version of equation (3) (see  
154 Section 3), along with parameterizations of mixing in the surface (Large et al. 1994) and bottom  
155 boundary layers and/or overflows (Legg et al. 2006; Danabasoglu et al. 2010), and mixing from  
156 resolved shear (Large et al. 1994; Jackson et al. 2008). These parameterizations produced spa-  
157 tially and temporally varying diapycnal diffusivities, with bottom enhancement and stratification  
158 dependence. However, these simulations did not include an energetically consistent representation  
159 of internal tide breaking away from the generation site; explicit representation of mixing from in-  
160 ternal waves generated by winds and sub-inertial flows; nor spatial and temporal variability in the

161 dissipation vertical profile. The work described here has revolved around developing and testing  
 162 energetically consistent, spatially and temporally variable mixing parameterizations. The result-  
 163 ing parameterizations are based upon internal gravity wave dynamics and the patterns of wave  
 164 generation, propagation, and dissipation.

### 165 *c. Overall strategy and philosophy of the CPT approach*

166 As with previous CPTs, we have found that parameterizations are most productively developed  
 167 when there is a broad base of knowledge that is in a state of *readiness* to be consolidated, imple-  
 168 mented and tested. Much of the basic research described here was published or nearing comple-  
 169 tion at the time this project started, allowing for a focused effort on parameterization development,  
 170 model implementation and global model testing. A key CPT component was the inclusion of four  
 171 dedicated post-doctoral scholars, who formed “the glue” to bridge the expertise of different prin-  
 172 cipal investigators, promoting projects at the intersection of theory and models, observations and  
 173 simulations, while gaining valuable broad training and networking.

174 One of the important tenets of the CPT is the consistent use of energy, power and the turbulent  
 175 kinetic energy dissipation rate  $\varepsilon$  (dimensions of  $L^2 T^{-3}$ ), rather than diapycnal diffusivity, as the  
 176 currency of turbulent mixing.  $\varepsilon$  describes the rate at which turbulence dissipates mechanical en-  
 177 ergy at the smallest scales. It is typically related to a diapycnal diffusivity through a dimensionless  
 178 mixing efficiency ( $\Gamma$ ), following Osborn (1980)

$$\kappa = \frac{\Gamma \varepsilon}{N^2}, \quad (2)$$

179 where  $N^2$  is the squared buoyancy frequency. Equation (2) shows that keeping the diffusivity fixed  
 180 in a world with changing stratification implies changes in energy dissipation in ways that are not  
 181 always consistent with the physical processes supplying energy for dissipation. We can overcome

182 this problem by formulating parameterizations directly in terms of  $\varepsilon$ . This approach also has the  
183 advantage of providing a transparent connection to dynamical processes driving mixing, since  
184 the downscale energy cascade can be directly linked to constraints of total power available for  
185 turbulence and other facets of ocean energetics (e.g., St. Laurent and Simmons 2006; Ferrari and  
186 Wunsch 2009). The topic of an appropriate value for mixing efficiency has had a resurgence of  
187 interest in recent years. Some theoretical and numerical studies suggest that a mixing efficiency  
188 that is systematically lower in areas of low ocean stratification might bias the type of global mixing  
189 estimates presented here and require modifications to model parameterizations (Mashayek et al.  
190 2013; Venayagamoorthy and Koseff 2016; Salehipour et al. 2016). A careful evaluation of mixing  
191 efficiency was not part of the CPT work, and a thorough discussion is beyond the scope of this  
192 paper. Interested readers are instead referred to recent reviews such as Peltier and Caulfield (2003)  
193 and Gregg et al. (2017).

## 194 **2. Global patterns and constraints**

195 Many of the early parameterizations described in Section 1b were motivated by individual pro-  
196 cess experiments or observational studies. At the same time, the novel observations, theories, and  
197 model results that fundamentally drive the field forward frequently arise unexpectedly, from pro-  
198 grams funded by many agencies. For example, the long-range propagation of coherent internal  
199 tides was discovered in both the ATOC (Acoustic Thermometry of Ocean Climate; Dushaw et al.  
200 (1995)) and satellite altimeter (Ray and Mitchum 1996) datasets fortuitously—neither mission was  
201 set up with a focus on internal tides.

202 Another factor contributing to the readiness of this CPT was the increased use of new techniques  
203 to infer mixing rates indirectly from a wide variety of data sources, allowing the rich patterns like  
204 those in Figure 2 to emerge. There are now enough direct microstructure and indirect estimates of

205 turbulent dissipation rates and diapycnal diffusivities to examine depth and geographical patterns,  
206 temporal variability and global budgets (Waterhouse et al. 2014). These patterns in turn have  
207 inspired new insights on the underlying dynamics driving and energetically supplying small-scale  
208 turbulence, and provided valuable constraints on modeled turbulent mixing rates. Compilation  
209 of both direct microstructure measurements and indirect estimates of turbulence is discussed in  
210 Section 7. Here we briefly describe recent results related to global patterns and statistics.

211 The average strength of turbulent diapycnal mixing appears to be roughly consistent, within  
212 error bars, with that ‘required’ to raise the deep waters of the global meridional overturning circu-  
213 lation (MOC). Using the most comprehensive-to-date collection of full-depth microstructure data,  
214 Waterhouse et al. (2014) report a globally-averaged diapycnal diffusivity below 1000 m depth of  
215  $\mathcal{O}(10^{-4} \text{ m}^2 \text{ s}^{-1})$  and above 1000 m depth of  $\mathcal{O}(10^{-5} \text{ m}^2 \text{ s}^{-1})$ . These values are consistent with  
216 the global inverse estimate of Lumpkin and Speer (2007). Using an indirect finescale approach  
217 (Section 7c), but with a much larger dataset, Kunze (2017) finds a global depth-averaged value  
218 of  $0.3 - 0.4 \times 10^{-4} \text{ m}^2 \text{ s}^{-1}$ . It is unclear whether any remaining differences between these esti-  
219 mates are due to sampling biases of the more limited microstructure data, to method biases of the  
220 finescale technique, or to assumptions of a fixed mixing efficiency.

221 The associated globally-averaged turbulent dissipation rates inferred from these observations  
222 cluster around  $2 \pm 0.6 \text{ TW}$  (Waterhouse et al. 2014; Kunze 2017). Given an assumed mixing  
223 efficiency, these rates are roughly consistent with estimates of power going through the three  
224 primary mechanisms of internal wave generation: barotropic tidal flow over topography leading  
225 to internal tides ( $\sim 1 \text{ TW}$ , see Sections 3 and 4); low-frequency flows over topography producing  
226 internal lee waves (0.2–0.7 TW, see Section 5); and variable wind forcing producing near-inertial  
227 internal waves ( $\sim 0.3\text{--}1 \text{ TW}$ , see Section 6).



228 Much more striking than average values is the enormous range and richness of the patterns visi-  
229 ble in Figure 2. Both the turbulent dissipation rate and diapycnal diffusivity vary by several orders  
230 of magnitude across ocean basins. Understanding how such patterns convolve with pathways of  
231 water mass movement, air-sea heat gain/loss, greenhouse gas input, and nutrient availability is the  
232 next frontier in interpreting diapycnal mixing in the ocean.

233 Many of these patterns (in space and time) can be interpreted in terms of the geography of in-  
234 ternal wave generation, propagation, and dissipation (Figure 1). Patterns immediately visible in  
235 Figure 2 include elevated values associated with more complex topography such as that associated  
236 with the western Indian, western and central Pacific and slow mid-ocean spreading ridges (Wi-  
237 jesekera et al. 1993; Polzin et al. 1997; Kunze et al. 2006; Decloedt and Luther 2010; Wu et al.  
238 2011; Whalen et al. 2012; Waterhouse et al. 2014). Over rough or steep topography, turbulence is  
239 frequently bottom-enhanced (Polzin et al. 1997; Waterhouse et al. 2014), but sometimes extends  
240 all the way up through the pycnocline (Kunze 2017). The temporal variability of diapycnal mixing  
241 shows seasonal (Whalen et al. 2012) and tidal cycles related to the two major internal wave energy  
242 sources, the winds and tides, as well as isolated events.

243 What follows in the sections below concerns first the main science efforts to consolidate our un-  
244 derstanding of turbulence from (i) mixing elevated over rough topography related to internal wave  
245 generation by tides, (ii) low-frequency flows that generate internal lee waves, and (iii) near-inertial  
246 internal wave generation by winds. In each section we describe the consequences of parameter-  
247 izing these processes in ocean climate models. For tides we subdivide our efforts into turbulence  
248 in the ‘nearfield’ of internal tide generation sites (loosely within one mode-one bounce) and the  
249 ‘farfield’ (waves that have propagated considerably further before breaking). Following that we  
250 describe tools developed through the CPT now made available to the wider community; namely  
251 (1) a uniquely comprehensive database of microstructure data, (2) techniques for analyzing ob-

servational data, and (3) new parameterizations of turbulence available for a variety of model implementations. We also briefly discuss the state of the art for high-resolution ocean models, which are beginning to partially resolve the internal gravity wave continuum on a global scale. We conclude this paper with thoughts for the future.

### 3. Nearfield tidal mixing

#### a. Physical motivation

Tidal frequency internal waves, generated by barotropic tidal flow over topographic obstacles in a stably stratified fluid, lead to local mixing near the generation site, both due to direct wave breaking (close to topography) and enhanced rates of interaction with other internal waves (well above topography). The formulation of St. Laurent et al. (2002) represented the enhanced turbulent dissipation rate as the product of the rate of conversion of barotropic tidal energy into internal waves,  $C$ ; the fraction of that energy which is ‘locally’ dissipated,  $q$  (note that consequently  $1 - q$  propagates away as low-mode internal tides); and a vertical distribution function of that local dissipation,  $F(z)$ . Through the Osborn relation in equation (2) (Osborn 1980), the enhanced turbulence is then related to a diffusivity as

$$\kappa = \kappa_b + \frac{q \Gamma C(x, y) F(z)}{\rho N^2}, \quad (3)$$

where  $\kappa_b$  is a place-holder background diffusivity. The conversion rate,  $C$ , is dependent on topographic roughness, tidal velocity, and bottom stratification (Bell 1975; Jayne and St. Laurent 2001; Garrett and Kunze 2007) (Figure 3c). St. Laurent et al. (2002) proposed a value of  $q = 1/3$ , and a function  $F(z)$  that decayed exponentially with height above topography, with a 500 m e-folding scale. They based these choices on analysis from several deep-ocean microstructure datasets. These values were used in climate model implementations, such as Simmons et al. (2004b), Jayne

(2009), Dunne et al. (2012), and Danabasoglu et al. (2012). The background diffusivity,  $\kappa_b$ , accounts for the mixing associated with energy that radiates from internal-tide generation sites, as well as other internal wave processes. Treatments of  $\kappa_b$  have varied, including: (i) a constant value of  $1 \times 10^{-5} \text{ m}^2 \text{ s}^{-1}$  (Simmons et al. 2004b; Jayne 2009), (ii) a latitudinal function capturing the equatorward decrease in wave-wave interactions (Henyey et al. 1986; Harrison and Hallberg 2008; Jochum 2009; Danabasoglu et al. 2012), and (iii) a stratification-dependent function after Gargett (1984) (used in Dunne et al. (2012)). Due to the sensitivity of the simulations to the different parameterizations, a major goal of the CPT has been to better understand and represent the physical processes that determine spatial and temporal variations in the parameters in equation (3).

A few estimates of  $q$  have been obtained, involving synthesis of observations and models. The radiated portion  $1 - q$  may be computed as the energy radiated out of a control volume  $\int \mathbf{J} \cdot \hat{\mathbf{n}} dA$ , where  $\mathbf{J}$  is the internal wave energy flux, divided by an estimate of the conversion rate  $C$ . Alternately, a direct estimate is from the integrated dissipation rate over that same volume,  $\int \rho \Gamma \epsilon dV / C$ . The observational sampling requirements for both estimates, particularly the second, are considerable. At the Hawaiian ridge, Klymak et al. (2006) obtained  $q = 0.15$  using the second method, as compared to an estimate of  $q < 0.5$  obtained with the first (Rudnick et al. 2003).

Existing theoretical predictions for  $C$ , summarized in Garrett and Kunze (2007) and Green and Nycander (2013), show dependence on topographic steepness relative to the internal tide characteristic steepness  $\gamma = (dh/dx)/s$  (where  $s = \sqrt{(f^2 - \omega^2)/(N^2 - \omega^2)}$ ,  $dh/dx$  is the topographic gradient,  $\omega$  is the wave frequency and  $f$  the Coriolis parameter), as well as the ratio of tidal excursion distance to topographic width. At supercritical rough topography ( $\gamma > 1$ ) the conversion rate saturates (Balmforth and Peacock 2009; Zhang and Swinney 2014) compared to linear theory applicable at subcritical topography ( $\gamma < 1$ ) (Bell 1975). Estimates of  $C$  need to include the contribution of abyssal hill topography, on scales  $\mathcal{O}(< 10 \text{ km})$  not resolved by current topography

297 products. Small-scale topography may increase  $C$  by 10% globally and 100% regionally (Melet  
298 et al. 2013b) (see Figure 3c).

299 A global constraint on the nearfield internal tide dissipation can be obtained from comparisons  
300 of satellite observations of internal tides with global simulations at  $\mathcal{O}(10\text{ km})$  resolution that in-  
301 clude realistic surface tidal forcing (Simmons et al. 2004a; Arbic et al. 2004, 2010; Niwa and  
302 Hibiya 2011; Müller et al. 2012; Shriver et al. 2012; Niwa and Hibiya 2014; Shriver et al. 2014;  
303 Waterhouse et al. 2014; Ansong et al. 2015; Buijsman et al. 2016; Rocha et al. 2016). All of these  
304 model runs explicitly simulate generation of low-mode tides, with horizontal scales  $> \mathcal{O}(50)\text{ km}$ .  
305 Some studies conducted since 2010 have also included concurrent atmospheric forcing, allowing  
306 for a more realistic, geographically varying background stratification field. In some of the models  
307 above, conversion to unresolved high modes, assumed to dissipate locally, is performed by a lin-  
308 ear wave drag based on linear theory (Bell 1975). Buijsman et al. (2016) find that modeled and  
309 observed internal tides show most agreement when about 60% of the energy converted to both low  
310 and high modes is dissipated close to the generation sites.

311 The vertical structure of associated turbulence appears to vary between deep rough topography,  
312 and tall steep topography, reflecting differences in the underlying physics driving turbulence. At  
313 tall steep ridges much of the baroclinic energy is contained in larger length scales that propagate  
314 away horizontally without breaking (St. Laurent and Nash 2004). Local mixing occurs through  
315 tidally generated transient arrested lee waves (Legg and Klymak 2008; Klymak et al. 2010; Al-  
316 ford et al. 2014) (Figure 3b), which might imply a  $q$  scaling with the barotropic flow speed  $U$ ,  
317 and an exponentially decaying vertical dissipation profile with lengthscale  $U/N$ . At the Kaena  
318 ridge, Hawaii, this theory suggests  $q \sim 7\%$ , less than the  $q \sim 15\%$  values estimated from observa-  
319 tions (Klymak et al. 2006). Interference with remotely generated internal tides modifies the local  
320 dissipation (Buijsman et al. 2012, 2014; Klymak et al. 2013); resonance between internal tides

321 generated at adjacent ridges (e.g. Luzon Straits) can increase local dissipation up to 40% (Alford  
322 et al. 2015). The percentage of local dissipation may be systematically higher in marginal seas  
323 or areas where lower modes are not free to escape (St. Laurent 2008; Nagai and Hibiya 2015).  
324 Similarly, nearfield tidal dissipation can be increased by topographically trapped internal waves  
325 generated by subinertial tidal constituents (Tanaka et al. 2013); i.e., the diurnal constituents at  
326 latitudes  $> 30^\circ$ , and the semidiurnal constituents at latitudes  $> 74.5^\circ$ . The energy density in such  
327 trapped motions increases with latitude, and is all dissipated locally (Musgrave et al. 2016).

328 At deep rough topography a variety of processes facilitate local wave breaking (Figure 3a).  
329 Wave-wave interactions can transfer energy to smaller scale waves that are more likely to break  
330 (McComas 1977; Müller et al. 1986; Henyey et al. 1986). This process is modeled in Polzin  
331 (2004b) with a one-dimensional radiation balance equation, resulting in an algebraically decay-  
332 ing dissipation profile with a spatially varying decay scale that matches Brazil Basin observations  
333 (Polzin et al. 1997) (Figure 3d). For small scale waves generated over subcritical abyssal hill  
334 topography, overturning of the upward propagating waves (Muller and Bühler 2009), predicts a  
335 bottom intensified dissipation, with a steeper than exponential decay with height and a local dissi-  
336 pation fraction as large as 60%. At and just below a critical latitude where the Coriolis frequency  
337 is half the tidal frequency, particularly efficient wave-wave interactions of a parametric subhar-  
338 monic instability type lead to a dissipation profile with high values extending several hundred  
339 meters above the bottom, before decaying rapidly to background levels, and  $q > 0.4$  (MacKinnon  
340 and Winters 2003; Ivey et al. 2008; Nikurashin and Legg 2011). Internal tide energy can also be  
341 transferred to smaller scales in the pycnocline, and by scattering from rough topography following  
342 reflection from the upper surface (Buhler and Holmes-Cerfon 2011). The value of  $q = 0.3$  used  
343 in existing parameterizations is therefore likely to be an under-estimate in many places, while an  
344 over-estimate in some.

345 *b. New parameterizations*

346 A major effort in the CPT and elsewhere has been to build upon the work of Jayne and St.  
 347 Laurent (2001) and St. Laurent et al. (2002) by deriving more dynamically variable and accurate  
 348 representations of both the decay profile,  $F(z)$ , and the fraction of locally dissipated wave energy,  
 349  $q$ . For deep, rough topography, Polzin (2009) formulates a parameterization of internal tide dissipa-  
 350 tion based on 1-D radiation balance equations with nonlinear closure. His formulation yields a  
 351 dissipation that scales like  $\varepsilon = \varepsilon_0 / (1 + z/z_p)^2$ , where  $z$  is the height above bottom (Figure 3d). In  
 352 Melet et al. (2013a) the scale height  $z_p$  is written in the form

$$z_p = \mu \left( \frac{U (N_b^{\text{ref}})^2}{h^2 k^2 N_b^3} \right) \quad (4)$$

353 where  $\mu$  is a non-dimensional constant,  $N_b^{\text{ref}}$  is a reference bottom buoyancy frequency, and  $U$ ,  $h$ ,  $k$ ,  
 354 and  $N_b$  are respectively the barotropic velocity, topographic roughness, topographic wavenumber,  
 355 and bottom buoyancy frequency for the particular location. WKB scaling contributes to the role  
 356 of stratification in (4). Another global map of  $q$  and vertical profile of dissipation for small-scale  
 357 rough topography has been generated by Lefauve et al. (2015) using the overturn mechanism of  
 358 Muller and Bühler (2009).

359 For turbulence at tall, steep slopes, a new parameterization of the near-field mixing due to tran-  
 360 sient arrested lee-waves (Klymak et al. 2010) uses linear theory for knife-edge ridge topography to  
 361 estimate baroclinic energy conversion into each mode (Llewellyn Smith and Young 2003). Those  
 362 modes with phase speeds less than the barotropic velocity at the top of the ridge are assumed to be  
 363 arrested, leading to local dissipation. Combining the total energy loss with a vertical length scale  
 364 of  $U/N$  produces a dissipation rate which decays exponentially away from the ridge top.

365 *c. Consequences for large-scale circulation*

366 Melet et al. (2013a) compare two simulations with the same formulation for internal-tide energy  
367 input but using different vertical profiles of dissipation (the St. Laurent et al. (2002) and Polzin  
368 (2009) formulations, also included in the Community Earth System Model, CESM). They used the  
369 GFDL CM2G coupled climate model with an isopycnal vertical coordinate in the ocean (Dunne  
370 et al. 2012). With the Polzin formulation, diffusivities are higher around 1000–1500 m, and lower  
371 in the deep ocean, resulting in modifications to the ocean stratification and changes of  $\mathcal{O}(10\%)$  in  
372 the meridional overturning circulation (Figure 3e).

373 Additional enhancements in the CESM ocean component, meant to improve the representation  
374 of tidally-driven mixing, include: separate treatment of diurnal and semi-diurnal tidal constituents  
375 and implementation of a subgrid-scale bathymetry parameterization that better resolves the verti-  
376 cal distribution of the barotropic energy flux, following Schmittner and Egbert (2014); alternative  
377 tidal dissipation energy data sets from Egbert and Ray (2003) and Green and Nycander (2013);  
378 and introduction of the 18.6-year lunar nodal cycle on the tidal energy fields. The global cli-  
379 mate impacts of these new enhancements are found to be rather small. However, there are local  
380 improvements such as a reduction in the warm bias in the upper ocean in the Kuril Strait region.

381 *d. Future work*

382 Ongoing work is synthesizing existing ideas for the dependence of  $q$  on topographic and flow  
383 parameters into a single global model for a spatially and temporally varying  $q$ , and incorporating  
384 these ideas into simulations. Comparison with additional observations of the strength and vertical  
385 decay scale of turbulence over rough topography is also desirable. For example, Kunze (2017) find  
386 that inferred dissipation rates over some topographic features extend upwards well into the ther-

387 mocline without appreciable decay. Parameterization of mixing by trapped tidally forced waves  
388 (perhaps especially important in the Arctic and Antarctic) also deserves dedicated attention.

#### 389 **4. Farfield internal tides**

390 About 20–80% of the internal tide energy is not dissipated near topographic sources (Section 3),  
391 and instead radiates away as low-mode internal waves. Satellite altimetry shows that these low-  
392 mode internal tides may propagate for thousands of kilometers from sources such as the Hawaiian  
393 Ridge (Figure 4a; Zhao et al. (2016)). This section examines where and how these low-modes  
394 dissipate, and parameterizations of this dissipation. Several mechanisms have been hypothesized  
395 as potential dissipators of farfield internal tides, including: interactions with rough topography  
396 (Johnston and Merrifield 2003; Mathur et al. 2014), interactions with mean flows and eddies (St.  
397 Laurent and Garrett 2002; Rainville and Pinkel 2006; Dunphy and Lamb 2014; Kerry et al. 2014),  
398 cascade to smaller scales via wave-wave interactions (McComas 1977; Müller et al. 1986; Henyey  
399 et al. 1986; Lvov et al. 2004; Polzin 2004a), including the particular subset of wave interactions  
400 known as parametric subharmonic instability (PSI) (Staquet and Sommeria 2002; MacKinnon and  
401 Winters 2005; Alford et al. 2007; Alford 2008; Hazewinkel and Winters 2011; MacKinnon et al.  
402 2013b,c; Simmons 2008; Sun and Pinkel 2012, 2013), or evolution on continental slopes and  
403 shelves (Nash et al. 2004, 2007; Martini et al. 2011; Kelly et al. 2013; Waterhouse et al. 2014).  
404 Here we summarize current understanding from theoretical and process studies and observational  
405 campaigns, recent parameterization developments, and consequences of farfield dissipation for  
406 global ocean models.



#### 407 *a. Observations*

408 The reflection, scattering, and dissipation of long-range low-mode internal tides have been ob-  
409 served at a few large topographic features. Satellite altimetry indicates scattering of mode-1 tides  
410 to higher modes along the Line Islands Ridge, 1000 km south of Hawaii (Johnston and Merrifield  
411 2003). Moored observations show significant reflection for mode-1 diurnal internal tides (but weak  
412 reflection for semidiurnal) at the South China Sea continental shelf (Klymak et al. 2011). Scat-  
413 tering of internal tides from low to high modes, and associated mixing, has been observed on the  
414 Virginia and Oregon continental slopes (Nash et al. 2004; Kelly et al. 2012; Martini et al. 2013). In  
415 contrast, at the steeper Tasmanian continental slope mode-1 internal tides appear to reflect without  
416 significant energy loss (Johnston et al. 2015).

#### 417 *b. Theory and numerical simulations*

418 The interaction between low-mode internal waves and large-amplitude topography, such as con-  
419 tinental slopes or tall isolated ridges, is strongly dependent on the steepness of the topography  
420 (Cacchione and Wunsch 1974; Johnston and Merrifield 2003; Legg and Adcroft 2003; Venayag-  
421 amoorthy and Fringer 2006; Helfrich and Grimshaw 2008; Hall et al. 2013; Legg 2014; Mathur  
422 et al. 2014). Shoaling subcritical topography can increase wave amplitude, increasing the Froude  
423 number (defined in Section 5) and causing wave breaking. Supercritical topography reflects low-  
424 mode waves back towards deeper water, with only small energy loss to dissipation (Klymak et al.  
425 2013). Near-critical topography scatters incident low-mode energy to much smaller wavelengths,  
426 leading to wave breaking and turbulence (Wunsch 1969; Ivey and Nokes 1989; Slinn and Riley  
427 1996; Ivey et al. 2000) concentrated near the sloping topography. Kelly et al. (2013) estimated the  
428 fraction of incoming mode-1 energy flux transmitted, reflected and scattered into higher modes  
429 for 2-dimensional sections across the continental slope for the entire global coastline. Three-

dimensional topographic variations such as canyons, cross-slope ridges and troughs, and bumps may enhance the local dissipation of the low-mode tide.

*c. Parameterizing farfield tides: a wave drag approach*

In global simulations of the HYbrid Coordinate Ocean Model (HYCOM) with realistic atmospheric and tidal forcing (Arbic et al. 2010), the resolved internal waves lose energy to a wave drag applied to flow in the bottom 500 m (see Section 3). This drag can be regarded as a parameterization of low- to high-mode scattering, and these high modes are assumed to dissipate at the generation site, within 500 m above the bottom topography. Comparison of the simulated  $M_2$  internal-tide SSH amplitudes in  $1/12.5^\circ$  HYCOM with satellite altimetry (Shriver et al. 2012; Ansong et al. 2015; Buijsman et al. 2016), shows that the open ocean wave drag is necessary to achieve agreement between modeled and observed barotropic and baroclinic tides, confirming the need for deep ocean dissipation of the low mode internal tides. Figures 4b and 4c, taken from Ansong et al. (2017), display the internal tide conversion rates and fluxes in HYCOM, and the comparison of HYCOM fluxes to fluxes in high-vertical-resolution moorings in the North Pacific (Zhao et al. 2010). Consistent with earlier studies, such as Simmons et al. (2004a), the conversion map shows that internal tides are generated in areas of rough topography such as the Hawaiian Ridge. The HYCOM-mooring comparison map in Figure 4c indicates that the HYCOM simulations are able to predict tidal fluxes with some reasonable degree of accuracy. Buijsman et al. (2016) found that about 12 % of these low modes reach the continental slopes, compared to 31 % found by Waterhouse et al. (2014). The HYCOM results cited above suggest the necessity of parameterized energy loss; but the current wave drag formulation used in HYCOM is based only upon topographic scattering, motivating additional studies to understand a greater number of relevant physical mechanisms implicated in the damping of farfield internal tides.

453 *d. Parameterizing farfield internal tides: a ray-tracing approach*

454 To represent the geography of farfield internal tide dissipation in a physically-based manner,  
455 the propagation, reflection and dissipation of low-mode energy must be parameterized in a GCM.  
456 A new numerical framework employs a vertically-integrated radiation balance equation to pre-  
457 dict the horizontal propagation of low-mode energy, simplifying earlier surface and internal wave  
458 modeling (e.g., WAMDI-Group 1988; Müller and Natarov 2003). In this approach, only the low-  
459 est modes are considered. Energy in each mode of each relevant tidal frequency is considered  
460 independently (or adiabatically), assuming minimal mode-mode energy transfer. Waves propa-  
461 gate horizontally with refraction due to variations in Coriolis, depth and stratification, invoking  
462 classic ray-tracing equations for long internal gravity waves (Lighthill 1976). Effects of back-  
463 ground flow (Rainville and Pinkel 2006) are currently neglected, but will be included in future  
464 versions. The  $1 - q$  fraction of the outgoing internal tide energy that does not dissipate locally  
465 (see Section 3) forms the source term in the radiation balance equation, and various parameteriza-  
466 tions for dissipation can be “plugged into” the framework as sink terms. Dissipation mechanisms  
467 currently considered include scattering at small-scale roughness (Jayne and St. Laurent 2001),  
468 quadratic bottom drag (similar to some of the simulations in Ansong et al. (2015)), and Froude  
469 number-based breaking (Legg 2014). A scheme for partial reflection at continental slopes uses the  
470 reflection coefficients of Kelly et al. (2013). This framework, currently implemented in GFDL’s  
471 MOM6 ocean model, can be adapted or extended to incorporate new parameterizations of sink and  
472 source phenomena. Eden and Olbers (2014) have developed a similar approach for propagating  
473 low-mode energy, with scattering to a high-mode continuum due to wave-wave interaction and  
474 topographic roughness (not including reflection at continental slopes).

475 *e. Consequences of farfield dissipation in GCMs*

476 To examine the sensitivity of large-scale ocean circulation to the location of farfield internal tide  
477 dissipation, a series of simulations were performed with the GFDL ESM2G coupled climate model  
478 (Dunne et al. 2012). These simulations (Melet et al. 2016) all have the same total energy input into  
479 the internal tide field, and the same magnitude and location of nearfield dissipation, with  $q = 0.2$   
480 and the bottom-intensified vertical profile described in St. Laurent and Garrett (2002). The re-  
481 maining 80 % of energy dissipation is distributed at one of three horizontal locations — deep  
482 basins, continental slope, coastal shelves — with one of three vertical dissipation profiles – dissi-  
483 pation which decays exponentially with height above bottom, scales like the buoyancy frequency  
484  $N$ , or like  $N^2$  (see Melet et al. (2016) for more detail). The resulting ocean circulation shows  
485 a significant dependence on the vertical profile of dissipation (Figures 4e and 4f). In particular,  
486 more dissipation in the upper ocean leads to stronger subtropical overturning cells, a broader ther-  
487 moclone, and higher thermosteric sea-level; more dissipation in the deep ocean leads to stronger  
488 deep meridional overturning circulation (more evidence of these impacts is shown in Melet et al.  
489 (2016)). In addition, the geographic location of the farfield dissipation influences the large-scale  
490 circulation notably when it impacts dense water formation regions: more dissipation on the slopes  
491 and shelves near the descending overflows tends to weaken the meridional overturning cell for  
492 which the lower branch is supplied by the overflows.

493 *f. Future work*

494 Future work on the ray-tracing approach should include refinement of the directional spectrum  
495 of radiated low-mode waves, including refraction by background flow, and evaluation of its im-  
496 pact in GCMs. Further work is also needed to understand and incorporate some of the detailed  
497 mechanisms of internal tide dissipation. One of these mechanisms is PSI, which may be especially

important near and equatorward of the diurnal turning latitudes  $\sim 29^\circ\text{N/S}$ . Note that the tide energy pathways via the tide constituents  $S_2$ ,  $O_1$ , and  $K_1$ , which collectively account for an amount of energy comparable to that of  $M_2$  (even greater, in some regions), need to be better understood. In particular, internal tides of various frequencies may have different responses to the same bottom topography and time-varying background flow. Progress here will involve a combination of relevant theory and observations with both idealized simulations and realistic tidally forced global simulations. Another dissipation pathway worthy of close attention is wave breaking and turbulence on continental slopes and shelves, where the vertical structure may be heavily influenced by details of wave dynamics in the presence of small-scale coastal topography, in ways that are not yet fully understood (e.g., Nash et al. 2007; Kunze et al. 2012; Wain et al. 2013; Pinkel et al. 2015; Waterhouse et al. 2017).

## 5. Internal lee waves

### *a. Theory and observations*

As with tides, mean flows over rough topography can generate internal waves that can remove energy and momentum from the large-scale circulation and, when they break, produce turbulent mixing (Figure 5a). Quasi-steady flow over small amplitude bathymetry ( $\gamma \lesssim 1/2$ , Nikurashin et al. (2014)) gives rise to vertically propagating internal lee waves of frequency  $Uk$ , where  $k$  is the topographic horizontal wavenumber and  $U$  is the mean flow speed. For large amplitude topography ( $\gamma \gtrsim 1/2$ ), the Froude number of the flow  $F = U/NH$  is  $\mathcal{O}(1)$ , such that topographic flow blocking and splitting becomes prominent: the flow transits the bump generating a non-propagating disturbance that converts parts of the flow kinetic energy to dissipation. Most of the real ocean lies between these two end cases (Bretherton 1969; Bell 1975; Pierrehumbert and

520 Bacmeister 1987; St. Laurent and Garrett 2002). The drag due to the combination of internal lee  
521 wave generation and topographic flow blocking and splitting is commonly denoted as wave drag  
522 in the atmospheric literature. Parameterizations of wave drag have been used for a long time in the  
523 atmospheric community (e.g. Palmer et al. 1986) but are less common in the ocean community.

524 Available global estimates for the energy conversion rate from geostrophic flows into internal lee  
525 waves range from 0.2 to 0.75 TW and highlight a prominent role of the Southern Ocean (Bell 1975;  
526 Nikurashin and Ferrari 2011; Scott et al. 2011; Wright et al. 2014). Several lines of evidence have  
527 suggested the existence of propagating lee waves (e.g., Naveira Garabato et al. 2004; St. Laurent  
528 et al. 2012; Waterman et al. 2013; Sheen et al. 2013, 2014; Clement et al. 2016) (Figure 5a). Yet,  
529 lee waves have not been definitively identified in ocean observations until recently, with Cusack  
530 et al. (2017) reporting unambiguous evidence of a lee wave in the Drake Passage (the search is  
531 complicated in part by the difficulty of observing motions with zero Eulerian frequency). Sparse  
532 observations also make it difficult to determine the fate of propagating lee waves. Non-propagating  
533 lee waves have been observed in a variety of fracture zones and deep passages (Ferron et al. 1998;  
534 Thurnherr et al. 2005; MacKinnon 2013; Alford et al. 2013), but their integrated importance to  
535 abyssal mixing is unknown.

#### 536 *b. Parameterizations and consequences of lee wave driven mixing on the ocean state*

537 The sensitivity of large-scale ocean circulation to lee wave driven mixing has been investigated  
538 in simulations with the GFDL ESM2G coupled climate model (Melet et al. 2014) using the esti-  
539 mated global map of energy conversion into lee waves of Nikurashin and Ferrari (2011) (Figure  
540 5b). The St. Laurent et al. (2002) exponential vertical structure was used as an initial placeholder  
541 for the structure of dissipation associated with breaking lee waves. Although most estimates put  
542 the global energy input into lee waves smaller than that into internal tides, Melet et al. (2014)

543 showed that lee wave-driven mixing significantly impacts the ocean state, yielding a reduction of  
544 the ocean stratification associated with a warming of the abyssal ocean. The lower cell of the  
545 MOC is also slightly lightened and increased in strength (Figure 5c). The different spatial dis-  
546 tribution of the internal tide and lee wave energy input is largely responsible for the sensitivity  
547 described in Melet et al. (2014), highlighting the previously reported importance of the patchiness  
548 of internal wave driven mixing in the ocean (e.g. Simmons et al. 2004a; Jayne 2009; Friedrich  
549 et al. 2011). Using a hydrographic climatology and a similar parameterization for lee wave driven  
550 mixing, Nikurashin and Ferrari (2013) and De Lavergne et al. (2016) also show substantial water  
551 mass transformation in the Southern Ocean due to internal lee wave driven mixing.

552 Trossman et al. (2013, 2016) implemented an inline wave drag parameterization (for both prop-  
553 agating and non-propagating lee waves) from the atmospheric community (Garner 2005) into a  
554 high-resolution ocean general circulation model (Figure 5d). The inline implementation allows  
555 for feedbacks between wave drag and the low-frequency flows that produce the lee waves. They  
556 found that the wave drag dissipated a substantial fraction of the wind energy input, significantly  
557 reduced both kinetic energy and stratification near the bottom, and reduced the model sea surface  
558 height variance and geostrophic surface kinetic energy by measurable amounts of  $\sim 20\%$ , while  
559 the performance of the model relative to in-situ and altimetric measurements of eddy kinetic en-  
560 ergy was not negatively impacted. Trossman et al. (2015) showed that dissipations predicted by  
561 the Garner (2005) scheme are not inconsistent with microstructure observations within the bottom  
562 500 meters in two Southern Ocean regions.

### 563 *c. Future work*

564 More observations are needed, especially in the Southern Ocean, to provide definitive evidence  
565 of the extent of propagating lee waves in the ocean, and further to explore (1) the fraction of

566 local dissipation and the vertical profile of dissipation of the propagating drag, (2) the relative  
567 importance of the propagating and non-propagating lee-wave drag, and (3) the observed mismatch  
568 between estimates of lee wave energy generation and near-bottom dissipation of lee waves.

569 Enhancing our knowledge of the near-bottom stratification and velocity fields and using a more  
570 accurate representation of topographic blocking are crucial for reducing our uncertainty about the  
571 global conversion rate into lee waves. Indeed, Wright et al. (2014) found that the use of different  
572 stratification products yields a difference of up to 0.25 TW in the global conversion rate into lee  
573 waves. Conversion rates are even more sensitive to the near-bottom velocity field (Trossman et al.  
574 2013; Melet et al. 2015), which can vary drastically with model resolution (Thoppil et al. 2011) and  
575 should take into account mesoscale eddy velocities. Topographic blocking accounts for most of  
576 the predicted dissipation by the Garner (2005) scheme in the bottom 1000 meters of two Southern  
577 Ocean domains (Trossman et al. 2015). Recent laboratory experiments by Dossmann et al. (2016)  
578 have shown that, for most forcing parameters they considered, nonlinear mixing mechanisms close  
579 to abyssal topography, such as topographic blocking, dominate the remote mixing mechanism  
580 by lee waves. Yet, theoretical conversion rates are highly sensitive to the choice of uncertain  
581 parameters related to the representation of topographic blocking and splitting (Nikurashin et al.  
582 2014).

583 As parameterized lee wave drag makes a significant impact on the ocean state (Trossman et al.  
584 2013, 2016), it should be included inline within climate models in a dynamically accurate manner  
585 to ensure credible ocean representation in a changing climate. Using linear theory and modeled  
586 resolved and parameterized bottom velocities and stratification, Melet et al. (2015) showed that the  
587 energy flux into lee waves exhibits a clear annual cycle in the Southern Ocean and that the global  
588 energy flux is projected to decrease by  $\sim 20\%$  from pre-industrial to future climate conditions  
589 under the RCP8.5 scenario. This time-variability is primarily due to changes in bottom velocities



590 (Melet et al. 2015). Ultimately, models should aspire to a full coupling between wind power,  
591 eddies and geostrophic circulations, stratification, and lee-wave drag and induced mixing. Such a  
592 coupling requires a state dependent, time evolving parametrization for the effects of lee waves.

## 593 **6. Wind-driven near-inertial motions**

### 594 *a. Theory and observations*

595 Much of what is known about wind-generated near-inertial waves (NIWs) builds on the observa-  
596 tions and model studies of the Ocean Storms Experiment (D’Asaro et al. 1995; Dohan and Davis  
597 2011); for a summary of the outcomes, other generation mechanisms and additional studies (see  
598 a review by Alford et al. (2016)). Inertial oscillations of the boundary layer are a free mode of  
599 the ocean and are its first response to changes in the wind stress (e.g. D’Asaro 1985). Part of the  
600 inertial oscillation energy is dissipated in the boundary layer through shear instability, thus con-  
601 verting kinetic energy to heat and potential energy (Large and Crawford 1995), with the remainder  
602 radiated away downward (Figure 6a) and equatorward (Figure 6b) in the form of propagating near-  
603 inertial internal waves (Alford 2003a; Plueddemann and Farrar 2006; Alford et al. 2012; Simmons  
604 and Alford 2012). The partition between high and low modes and the energy lost to dissipation at  
605 the mixed-layer base is unknown. In Ocean Storms, approximately one third of the energy input  
606 by the wind was carried away equatorward in modes one and two. Another study (Alford et al.  
607 2012) found a similar fraction was carried downward in higher modes, while a modeling study by  
608 Furuichi et al. (2008) found that only 10% reached past 150 m. Inferred global upper ocean dissi-  
609 pation rates show a clear seasonal cycle (Whalen et al. 2012), particularly in storm track latitudes  
610 (Whalen et al. 2015). Near-inertial KE at all depths also shows a clear seasonal cycle, indicating

611 that some of the energy makes it deep into the ocean (Alford and Whitmont 2007; Silverthorne  
612 and Toole 2009).

613 *b. Parameterizations and consequences*

614 The CPT tackled the upper ocean portion of the NIW related mixing with a three step process,  
615 described in Jochum et al. (2013), suitable for general use in coupled atmosphere-ocean models.  
616 Firstly, atmosphere and ocean models are coupled more frequently (e.g., two hours instead of  
617 daily), to allow resonant generation of near-inertial motions in the oceanic surface boundary layer.  
618 Even with high-frequency coupling, the near-inertial speeds can be too weak by 50% if the frontal  
619 structure of storms is not properly resolved by the atmospheric component of climate models. In  
620 such cases, the missing amplitude of the NIWs must be computed during the integration and added  
621 to the shear calculation of the boundary layer parameterization. The online computation of the  
622 near-inertial part of the velocity is not trivial, because during the integration the ocean model only  
623 has information about adjacent time steps. Fortunately, however, outside the deep tropics, velocity  
624 fluctuations from one model time step (e.g., one hour) to the next are mostly due to NIWs, which  
625 allows the accurate determination of near-inertial velocity during the integration (see Jochum et al.  
626 (2013) for details and method verification). Lastly, the air-sea flux of inertial wave energy into the  
627 boundary layer is determined, and 30% of it (Rimac et al. 2016) is used to increase the background  
628 diffusivity below the boundary layer. The energy in the last step is distributed with an exponential  
629 decay scale of 2000 m (Alford and Whitmont 2007). The resultant turbulent mixing from near-  
630 inertial motions changes the heat distribution in the upper ocean significantly enough to modify  
631 tropical SST patterns, and leads to a 20% reduction in tropical precipitation biases (Jochum et al.  
632 (2013); for the sensitivity of precipitation to the strength of near-inertial waves see Figures 6c and  
633 6d).

### 634 *c. Ongoing and future work*

635 Much hinges on the appropriate representation of NIWs. The largest uncertainties are associ-  
636 ated with the poorly known high frequency and wavenumber part of the wind spectrum, and the  
637 partitioning between locally dissipated energy and the amount radiated away. Thus, the energy  
638 available for NIW induced mixing in the surface boundary layer ranges from 0.3-1.0 TW (Alford  
639 2001, 2003b; Simmons and Alford 2012; Rimac et al. 2013). The Jochum et al. (2013) study was  
640 based on 0.34 TW; allowing for 0.68 TW in the Community Climate System Model would remove  
641 the spurious southern Intertropical Convergence Zone (ITCZ) and would result in a realistically  
642 shaped South Pacific Convergence Zone (Figure 6c). Thus, ongoing work focuses on the detailed  
643 analysis of moorings with co-located wind and ocean velocity measurements (e.g. Plueddemann  
644 and Farrar 2006; Alford et al. 2012).

## 645 **7. Tools and techniques**

### 646 *a. Microstructure database*

647 The CPT worked in conjunction with the CLIVAR & Carbon Hydrographic Data Office  
648 (CCHDO) at Scripps Institution of Oceanography to develop a standardized format for archiv-  
649 ing microstructure data. Data has been archived as CF-compliant NetCDF files with 1 m binned  
650 data (where possible). The database contains the following variables: time, depth, pressure, tem-  
651 perature, salinity, latitude, longitude, and bottom depth. The database also contains the newly  
652 designated variables: epsilon ( $\text{W kg}^{-1}$ ; *ocean turbulent kinetic energy dissipation rate*), and,  
653 when available, chi-t ( $^{\circ}\text{C}^2 \text{ s}^{-1}$ ; *ocean dissipation rate of thermal variance from micro-*  
654 *temperature*) and chi-c ( $^{\circ}\text{C}^2 \text{ s}^{-1}$ ; *ocean dissipation rate of thermal variance from microconductiv-*  
655 *ity*). Database entries include names of the project, project PIs and cruise information (research

656 ship, ports of entry and exit, cruise dates, chief scientist). Database entries have project spe-  
657 cific DOIs to cite the data in publications. Relevant cruise reports, project related papers and  
658 other documents are also contained in the data archive. At present, the database consists of 25  
659 separate projects and can be accessed at <http://microstructure.ucsd.edu>. Newly obtained  
660 microstructure data can be uploaded to the microstructure database by sending 1-m binned data to  
661 the CCHDO office at <http://cchdo.ucsd.edu/submit>.

662 *b. A repository for ocean mixing analysis tools, methods, and code*

663 The availability of commercially manufactured turbulence profilers, along with an increased  
664 use of mixing proxies, have expanded the size of the mixing community and the number of  
665 publications that use mixing observations. Many variants of processing code have thus been  
666 developed in parallel by different groups. Some variants have subtle differences in method-  
667 ology that can potentially lead to significant quantitative differences in the results. We thus  
668 sought to establish a community-based online repository for "best-practices" data analysis tools  
669 used for ocean mixing and internal wave calculations. Analysis code from many independent  
670 groups is available for download from the repository, thus facilitating comparison of techniques  
671 in an open, objective way. To accomplish this goal, a Github mixing repository was created  
672 (<https://github.com/OceanMixingCommunity/>) and populated with standard algorithms and  
673 process methods.

674 The goals of the public repository are to (1) enable reproducibility of analyses, (2) allow for  
675 comparison of different datasets using the same code, (3) provide a means for easy reanalysis if  
676 a bug is identified, or a best-practice change is suggested, (4) allow testing of one code against  
677 another version, and (5) provide a well-documented and version-controlled repository suitable for  
678 citation of techniques employed in publications. The code is primarily (but not exclusively) Matlab

679 based, and included routines for calculation of Thorpe scales,  $N^2$ , finescale parameterizations,  
680 generic and instrument-specific turbulence processing code, and sample data files.

681 *c. Observational data analysis: the fine-scale parameterizations*

682 Many of the insights described in this paper were inspired in part by the vast expansion of mix-  
683 ing data (e.g. Figure 2) that has come from widespread use of the ‘finescale’ parameterization for  
684 ocean mixing rates. Its increasing popularity warrants a few comments here. Finescale parame-  
685 terizations produce the average dissipation rate expected over several wave periods, and therefore  
686 are helpful in assessing the spatial and temporal mean dissipation rate or diffusivity. Inferences  
687 of mixing from finescale parameterizations are more extensive than instantaneous observations of  
688 turbulence from microstructure measurements (e.g. Polzin et al. 1996; Kunze et al. 2006; Whalen  
689 et al. 2012).

690 Finescale parameterizations rely on the fact that the observed shear and strain variance in the  
691 thermocline and below is mainly caused by internal waves. The parameterizations also assume  
692 that the energy dissipation rate is primarily due to non-linear interactions between internal waves  
693 that transfer energy from the finescale toward smaller-scale waves that subsequently break into  
694 turbulence. As discussed in Polzin et al. (2014), an expression of the down-spectrum energy  
695 cascade in the open ocean has been developed (Henyey et al. 1986; Müller et al. 1986; Henyey  
696 and Pomphrey 1983) in terms of the shear and strain spectra. This expression allows for estimates  
697 of the dissipation rate as a function of the spectra.

698 Parameterizations using finescale shear and strain profiles have been tested in a variety of con-  
699 texts, consistently demonstrating a factor of 2-3 agreement with microstructure inferences in open-  
700 ocean conditions (Gregg 1989; Polzin et al. 1995; Winkel et al. 2002; Polzin et al. 2014) and with  
701 strain-only inferences in a variety of locations (Wijesekera et al. 1993; Frants et al. 2013; Wa-

702 terman et al. 2014; Whalen et al. 2015). The shear- and strain-based parameterization is known  
703 to be less effective in regions where the underlying assumptions behind the parameterization do  
704 not apply (Polzin et al. 2014). These regions include continental shelves (Mackinnon and Gregg  
705 2003), strong geostrophic flow regimes over rough topography (Waterman et al. 2014), and regions  
706 with very large overturning internal waves (Klymak et al. 2008). Implementation of the parame-  
707 terizations in the open-ocean have revealed reasonable patterns and insight into the geography of  
708 diapycnal mixing using shear (Polzin et al. 1997; Kunze et al. 2006; Huussen et al. 2012) and strain  
709 (Kunze et al. 2006; Wu et al. 2011; Whalen et al. 2012). A global dissipation rate product that is  
710 based on both finestructure estimates and microstructure measurements is currently in preparation  
711 that will be made publicly available (C. Whalen).

#### 712 *d. Global internal wave models*

713 It has only been in the last decade that global models of internal waves have been developed  
714 (Arbic et al. 2004; Simmons et al. 2004a). As described above, several global internal wave  
715 models used in the community now include atmospheric and tidal forcing, enabling examination  
716 of many issues of interest such as the global three-dimensional internal wave geography, internal  
717 wave-mesoscale interactions, and an internal gravity wave continuum spectrum that approaches  
718 the observed continuum more closely as model resolution is refined (Müller et al. 2015).

#### 719 *e. The Community ocean Vertical Mixing (CVMix) package*

720 CVMix is a software package that provides transparent, robust, flexible, well-documented, and  
721 shared Fortran source codes for use in parameterizing vertical mixing processes in numerical ocean  
722 models. The project is focused on developing software for a consensus of first-order closures that  
723 return a vertical diffusivity, viscosity, and possibly a non-local transport (e.g., as in the K-Profile

724 Parameterization (KPP) scheme of Large et al. 1994), with each quantity dependent on the tracer  
725 or velocity being mixed. CVMix provides a software framework for the physical parameterizations  
726 arising from the internal-wave driven mixing CPT. For example, the Simmons et al. (2004b) tidal  
727 mixing scheme, available in CVMix, serves as a useful example for other tidal mixing schemes  
728 such as Melet et al. (2013a). Code development occurs within a community of scientists and  
729 engineers who make use of CVMix modules for a variety of ocean climate models (e.g., MPAS-O  
730 used at Los Alamos National Laboratory, POP used at NCAR, and MOM6 used at GFDL). CVMix  
731 modules are freely available to the community under GPLv2, using an open development approach  
732 on Github (<https://github.com/CVMix>). We solicit further contributions of parameterizations,  
733 thus enabling a very broad group of climate modelers to make use of the schemes.

## 734 **8. Summary and future science directions**

735 A frequently asked question related to this work is “Which mixing processes matter most for cli-  
736 mate?”. As with many alluringly comprehensive sounding questions, the answer is “it depends”.  
737 Deep ocean mixing matters for the decadal to centennial time-scales on which the deep, global  
738 circulation evolves. The mixing process most important for the deep circulation is the one with  
739 the most power, namely the tides. The distribution of mixing above deep rough topography from  
740 nearfield tidal dissipation is the most fully developed aspect of our work, both in terms of dy-  
741 namical understanding and parameterization implementation (Section 3, Figure 3). As detailed in  
742 Section 4, our understanding of farfield tidal dissipation is less complete. Lee waves may also con-  
743 tain significant power and play an important role in places like the Southern Ocean; preliminary  
744 results hint at a substantial role in water mass modification in this globally important region, but  
745 more observations and data-model-theory comparison is needed before we are confident of how  
746 best to represent them (Section 5, Figure 5). Non-propagating form drag is known to be important

747 for momentum budgets in the atmosphere, but has just begun to receive significant oceanographic  
748 attention (Trossman et al. 2016); it may be not only locally important for mixing tracers and mo-  
749 mentum wherever strong flow encounters sharp or rough topography, but a globally important  
750 drain of mesoscale energy.

751 Mixing in the main pycnocline can impact heat distribution and steric sea level rise on decadal  
752 time-scales, which makes it a compelling societal problem. Turbulent mixing in this depth range  
753 is controlled by a combination of downward-propagating near-inertial waves (Section 6, Figure  
754 6), low-mode, long-range-propagating internal tides breaking on continental slopes (Section 4,  
755 Figure 4), and by nearfield breaking of upward propagating internal tides or lee waves through  
756 nonlinear interactions. Double diffusion processes may also be significant in the main pycnocline  
757 (e.g. Schmitt et al. 2005), but are not covered here. For forward progress, a better understanding  
758 of low-mode wave breaking on slopes, with particular focus on the vertical structure of resultant  
759 dissipation (Carter and Gregg 2002; Nash et al. 2004, 2007; Martini et al. 2011; Kunze et al. 2012;  
760 Pinkel et al. 2015; Waterhouse et al. 2017), will help to constrain mixing rates.

761 It is increasingly clear that near-inertial wave driven mixing both below the surface boundary  
762 layer and down into the main thermocline is significantly mediated by the presence of mesoscale  
763 eddies. Areas of enhanced diffusivities have been linked to regions of elevated eddy kinetic energy,  
764 though the mechanisms are not always clear (e.g. Kunze et al. 1995; Whalen et al. 2012). In turn,  
765 interactions with internal waves may be a significant energy loss term for eddies (Buhler and  
766 McIntyre 2005; Polzin 2010; Whalen 2015; Barkan et al. 2017).

767 Mixing in the upper ocean matters to climate phenomena of seasonal to inter-annual, and perhaps  
768 even longer, time-scales. Turbulence beneath the surface boundary layer has a strong effect on  
769 upper ocean freshwater content and heat, and through SST changes, on a variety of coupled air-  
770 sea interactions ranging from the MJO to ENSO (e.g. Moum et al. 2016). In this depth range



771 (of order one hundred meters below the boundary layer), turbulence from breaking NIW plays a  
772 dominant role (Section 6, Figure 6). Again, the interaction with mesoscale eddies, and in particular  
773 mesoscale vorticity, may play a large role in setting the patterns and rates of wave propagation and  
774 dissipation in ways that are poorly constrained. We hope that continued work in this field will  
775 be closely coupled with the many active research programs focused on mixing parameterizations  
776 within the surface boundary layer, which may also be ripe for a CPT-style renovation.

777 Upper ocean mixing takes on a unique relevance at high latitudes. The presence of ice (either  
778 ice shelves or sea-ice) significantly changes both the dynamics and thermodynamics of turbulence  
779 near the poles, particularly in the near-surface ocean. Yet accurate representation of mixing in  
780 these environments is crucial if we are to accurately forecast everything from ice melt rates, to high  
781 latitude CO<sub>2</sub> absorption/outgassing, to deep water formation, to ecosystem responses to climate  
782 change. Multiple US funding agencies are increasingly putting substantial resources into process  
783 studies, long-term observations, and modeling. A formalized CPT-like framework might help  
784 bring these components together.

## 785 **9. Best practices for continuing success**

786 Once a field is in a state of readiness, where substantial observations, theory and dynamical  
787 understanding exist, the Climate Process Team structure or similar programs provide a productive  
788 template for progress. The CPT framework allows for (1) motivation to bring some parts of that  
789 research to a state of closure, (2) the opportunity to bring together observationalists, theorists and  
790 modelers to work through details of synthesizing observational reality, theoretical insights, and  
791 modeling efforts. The formal charge of CPT funding was essential to initiate this process and  
792 sustain it for the years necessary to bring such collaboration to productive fruition. A crucial  
793 component of this successful interaction has been the presence of dedicated personnel who pull

794 together the state of observational science and/or are embedded within modeling centers; post-  
795 docs or early career scientists fit well into this role. Similar facilitated cross-field collaborations  
796 are increasingly built into the structure of other multi-PI projects, best practices for which are  
797 well described by Cronin et al. (2009). At the same time, the epiphanies, new ideas and novel  
798 observations that fundamentally drive the field forward frequently come not from big science, but  
799 from a cornucopia of much smaller exploratory efforts and the continued small-scale development  
800 of innovative observing technology and numerical techniques. We must not lose the ability to be  
801 surprised.

802 *Acknowledgments.* We are grateful to US CLIVAR for their leadership in instigating and facil-  
803 itating the Climate Process Team program, NSF and NOAA for funding, and Eric Itsweire in  
804 particular for his steadfast support and enthusiasm. We thank Alistair J. Adcroft, Mike Levy,  
805 Brandon Reichl, Todd Ringler, and Luke Van Roekel for their contributions to the CVMix project;  
806 Peter Gent; and Andreas Schmittner and David Ullman for their contributions to the advances in  
807 tidal mixing parameterizations in the CESM ocean component. NCAR is sponsored by the NSF.

## 808 **References**

- 809 Alford, M. H., 2001: Internal swell generation: The spatial distribution of energy flux from the  
810 wind to mixed-layer near-inertial motions. *Journal of Physical Oceanography*, **31** (8), 2359–  
811 2368.
- 812 Alford, M. H., 2003a: Energy available for ocean mixing redistributed through long-range propa-  
813 gation of internal waves. *Nature*, **423**, 159–163.
- 814 Alford, M. H., 2003b: Improved global maps and 54-year history of wind-work on ocean inertial  
815 motions. *Geophys. Res. Lett.*, **30** (8), 1424–1427.

- 816 Alford, M. H., 2008: Observations of parametric subharmonic instability of the diurnal internal  
817 tide in the South China Sea. *Geophys. Res. Lett.*, **35** (L15602), doi:10.1029/2008GL034720.
- 818 Alford, M. H., M. F. Cronin, and J. M. Klymak, 2012: Annual Cycle and Depth Penetration of  
819 Wind-Generated Near-Inertial Internal Waves at Ocean Station Papa in the Northeast Pacific.  
820 *Journal of Physical Oceanography*, **42** (6), 889–909.
- 821 Alford, M. H., J. B. Girton, G. Voet, G. S. Carter, J. B. Mickett, and J. M. Klymak, 2013: Turbulent  
822 mixing and hydraulic control of abyssal water in the Samoan Passage. *Geophys. Res. Lett.*,  
823 **40** (17), 4668–4674.
- 824 Alford, M. H., J. M. Klymak, and G. S. Carter, 2014: Breaking internal lee waves at Kaena Ridge,  
825 Hawaii. *Geophys. Res. Lett.*, **41**, 906–912.
- 826 Alford, M. H., J. A. MacKinnon, H. L. Simmons, and J. D. Nash, 2016: Near-inertial internal  
827 gravity waves in the ocean. *Annual review of marine science*, **8**, 95–123.
- 828 Alford, M. H., J. A. MacKinnon, Z. Zhao, R. Pinkel, J. Klymak, and T. Peacock, 2007: Internal  
829 waves across the Pacific. *Geophys. Res. Lett.*, **34** (L24601), doi:10.1029/2007GL031566.
- 830 Alford, M. H., and M. Whitmont, 2007: Seasonal and spatial variability of near-inertial kinetic  
831 energy from historical moored velocity records. *Journal of Physical Oceanography*, **37** (8),  
832 2022–2037.
- 833 Alford, M. H., and Coauthors, 2015: The formation and fate of internal waves in the South China  
834 Sea. *Nature*, **521**, DOI:10.1038/nature14399.
- 835 Ansong, J. K., B. K. Arbic, M. C. Buijsman, J. G. Richman, J. F. Shriver, and A. J. Wallcraft,  
836 2015: Indirect evidence for substantial damping of low-mode internal tides in the open ocean.  
837 *Journal of Geophysical Research: Oceans*, **120** (9), 6057–6071.

- 838 Ansong, J. K., and Coauthors, 2017: Semidiurnal internal tide energy fluxes and their variability  
839 in a global ocean model and moored observations. *Journal of Geophysical Research: Oceans*,  
840 n/a–n/a, doi:10.1002/2016JC012184, URL <http://dx.doi.org/10.1002/2016JC012184>.
- 841 Arbic, B. K., S. T. Garner, R. Hallberg, and H. L. Simmons, 2004: The accuracy of surface  
842 elevations in forward global barotropic and baroclinic tide models. *Deep Sea Research Part II*,  
843 **51**, 3069–3101.
- 844 Arbic, B. K., A. J. Wallcraft, and E. J. Metzger, 2010: Concurrent simulation of the eddying  
845 general circulation and tides in a global ocean model. *Ocean Modelling*, **32 (3)**, 175–187.
- 846 Balmforth, N. J., and T. Peacock, 2009: Tidal conversion by supercritical topography. *Journal of*  
847 *Physical Oceanography*, **39**, 1965–1974.
- 848 Barkan, R., K. B. Winters, and J. C. McWilliams, 2017: Stimulated imbalance and the enhance-  
849 ment of eddy kinetic energy dissipation by internal waves. *Journal of Physical Oceanography*,  
850 **47 (1)**, 181–198.
- 851 Bell, T., 1975: Topographically generated internal waves in the open ocean. *Journal of Geophysi-*  
852 *cal Research*, **80**, 320–327.
- 853 Bretherton, F. P., 1969: Momentum transport by gravity waves. *Quarterly Journal of the Royal*  
854 *Meteorological Society* *quarterly journal of the royal meteorological society*, **95 (404)**, 213–243.
- 855 Bryan, K., and L. J. Lewis, 1979: A water mass model of the world ocean. *Journal of Geophysical*  
856 *Research*, **84**, 2503–2517.
- 857 Buhler, O., and M. Holmes-Cerfon, 2011: Decay of an internal tide due to random topography in  
858 the ocean. *J. Fluid Mech*, **678**, 271–293– doi:10.1017-jfm.2011.115.

859 Buhler, O., and M. McIntyre, 2005: Wave capture and wave-vortex duality. *Journal of Fluid*  
860 *Mechanics*, **534**, 67–96.

861 Buijsman, M., S. Legg, and J. Klymak, 2012: Double ridge internal tide interference and its effect  
862 on dissipation in Luzon Strait. *Journal of Physical Oceanography*, **42**, 1337–1356.

863 Buijsman, M. C., and Coauthors, 2014: Three-Dimensional Double-Ridge Internal Tide Reso-  
864 nance in Luzon Strait. *Journal of Physical Oceanography*, **44**, DOI:10.1175/JPO-D-13-024.1.

865 Buijsman, M. C., and Coauthors, 2016: Impact of internal wave drag on the semidiurnal energy  
866 balance in a global ocean circulation model. *Journal of Physical Oceanography*, **46**, 1399–1419,  
867 doi:10.1175/JPO-D-15-0074.1.

868 Cacchione, D., and C. Wunsch, 1974: Experimental study of internal waves over a slope. *Journal*  
869 *of Fluid Mechanics*, **66**, 223–239.

870 Carter, G. S., and M. C. Gregg, 2002: Intense, variable mixing near the head of Monterey Subma-  
871 rine Canyon. *Journal of Physical Oceanography*, **32**, 3145–3165.

872 Clement, L., E. Frajka-Williams, K. L. Sheen, J. A. Brearley, and A. C. Naveira Garabato, 2016:  
873 Generation of internal waves by eddies impinging on the western boundary of the North At-  
874 lantic. *Journal of Physical Oceanography*, **46**, 1067–1079.

875 Cronin, M. F., S. Legg, and P. Zuidema, 2009: Climate research: Best practices for process studies.  
876 *Bulletin of the American Meteorological Society*, **90** (7), 917–918.

877 Cusack, J. M., A. C. Garabato, D. A. Smeed, and J. B. Girton, 2017: Observation of a large lee  
878 wave in the drake passage. *Journal of Physical Oceanography*, **in press** (0), null, doi:10.1175/  
879 JPO-D-16-0153.1.

880 Danabasoglu, G., S. Bates, B. Briegleb, S. Jayne, M. Jochum, W. Large, S. Peacock, and S. Yeager,  
881 2012: The CCSM4 ocean component. *Journal of Climate*, **25**, 1361–1389.

882 Danabasoglu, G., W. Large, and B. Briegleb, 2010: Climate impacts of parameterized nordic sea  
883 overflows. *Journal of Geophysical Research*, **115**, C11005, doi:10.1029/2010JC006243.

884 D’Asaro, E., 1985: The energy flux from the wind to near-inertial motions in the mixed layer.  
885 *Journal of Physical Oceanography*, **15**, 943–959.

886 D’Asaro, E. A., C. E. Eriksen, M. D. Levine, P. Niiler, C. A. Paulson, and P. V. Meurs, 1995:  
887 Upper-ocean inertial currents forced by a strong storm, part I, Data and comparisons with linear  
888 theory. *Journal of Physical Oceanography*, **25**, 2909–2936.

889 De Lavergne, C., G. Madec, J. Le Sommer, A. G. Nurser, and A. C. Naveira Garabato, 2016:  
890 The impact of a variable mixing efficiency on the abyssal overturning. *Journal of Physical*  
891 *Oceanography*, **46** (2), 663–681.

892 Decloedt, T., and D. Luther, 2010: On a simple empirical parameterization of topography-  
893 catalyzed diapycnal mixing in the abyssal ocean. *Journal of Physical Oceanography*, **40** (3),  
894 487–508.

895 Dohan, K., and R. E. Davis, 2011: Mixing in the transition layer during two storm events. *Journal*  
896 *of Physical Oceanography*, **41** (1), 42–66.

897 Dossmann, Y., M. G Rosevear, R. W. Griffiths, G. O. Hughes, M. Copeland, and Coauthors, 2016:  
898 Experiments with mixing in stratified flow over a topographic ridge. *Journal of Geophysical*  
899 *Research: Oceans*, **121** (9), 6961–6977.

- 900 Dunne, J. P., and Coauthors, 2012: GFDL's ESM2 global coupled climate-carbon Earth System  
901 Models Part I: Physical formulation and baseline simulation characteristics. *Journal of Climate*,  
902 **25**, 6646—6665.
- 903 Dunphy, M., and K. G. Lamb, 2014: Focusing and vertical mode scattering of the first mode  
904 internal tide by mesoscale eddy interaction. *J. Geophys. Res. Oceans*, **119**, doi:doi:10.1002/  
905 2013JC009293.
- 906 Dushaw, B., B. Howe, B. Cornuelle, P. Worcester, and D. Luther, 1995: Barotropic and baro-  
907 clinic tides in the central North Pacific Ocean determined from long-range reciprocal acoustic  
908 transmissions. *Journal of Physical Oceanography*, **25**, 631–647.
- 909 Eden, C., and D. Olbers, 2014: An energy compartment model for propagation, non-linear inter-  
910 action and dissipation of internal gravity waves. *Journal of Physical Oceanography*, **44**, 2093–  
911 2106, doi:10.1175/JPO-D-13-0224.1.
- 912 Egbert, G. D., and R. D. Ray, 2003: Semi-diurnal and diurnal tidal dissipation from  
913 TOPEX/Poseidon altimetry. *Geophys. Res. Lett.*, **30**, 1907, doi:10.1029/2003GL017676, URL  
914 <http://dx.doi.org/10.1029/2003GL017676>.
- 915 Ferrari, R., and C. Wunsch, 2009: Ocean circulation kinetic energy: Reservoirs, sources, and  
916 sinks. *Annual Review of Fluid Mechanics*, **41** (1), 253–282, doi:10.1146/annurev.fluid.40.  
917 111406.102139.
- 918 Ferron, B. H., H. Mercier, K. Speer, A. Gargett, and K. Polzin, 1998: Mixing in the Romanche  
919 Fracture Zone. *Journal of Physical Oceanography*, **28**, 1929–1945.

Frants, M., G. M. Damerell, S. T. Gille, K. J. Heywood, J. A. Mackinnon, and J. Sprintall, 2013:  
An Assessment of Density-Based Finescale Methods for Estimating Diapycnal Diffusivity in  
the Southern Ocean. *Journal of Atmospheric and Oceanic Technology*, **30** (11), 2647–2661.

Friedrich, T., A. Timmermann, T. Decloedt, D. S. Luther, and A. Mouchet, 2011: The effect  
of topography-enhanced diapycnal mixing on ocean and atmospheric circulation and marine  
biogeochemistry. *Ocean Modelling*, **39**, 262–274.

Furuichi, N., T. Hibiya, and Y. Niwa, 2008: Model predicted distribution of wind-induced  
internal wave energy in the world's oceans. *J. Geophys. Res.*, **113** (C09034), doi:10.1029/  
2008JC004768.

Gargett, A. E., 1984: Vertical eddy diffusivity in the ocean interior. *Journal of Marine Research*,  
**42**, 359–393.

Garner, S. T., 2005: A topographic drag closure built on an analytical base flux. *Journal of Atmo-  
spheric Science*, **62**, 2302–2315.

Garrett, C., and E. Kunze, 2007: Internal tide generation in the deep ocean. *Annual Review of  
Fluid Mechanics*, **39**, 57–87.

Gaspar, P., Y. Gregoris, and J. Lefevre, 1990: A simple eddy kinetic energy model for simulations  
of the oceanic vertical mixing: Tests at station Papa and long-term upper ocean study site.  
*Journal of Geophysical Research*, **95**, 16 179–16 193.

Green, J. A. M., and J. Nycander, 2013: A comparison of tidal conversion parameterizations for  
tidal models. *Journal of Physical Oceanography*, **43**, 104–119.

Gregg, M., 1989: Scaling turbulent dissipation in the thermocline. *J. Geophys. Res.*, **94** (C7),  
9686–9698.



942 Gregg, M. G., E. A. D’Asaro, and J. J. Riley, 2017: Mixing coefficients and mixing efficiency in  
 943 the ocean. *Annual Reviews of Marine Science*, **(in press)**.

944 Griffies, S. M., R. C. Pacanowski, and R. W. Hallberg, 2000: Spurious diapycnal mixing associ-  
 945 ated with advection in a  $z$ -coordinate ocean model. *Monthly Weather Review*, **128**, 538–564.

946 Hall, R., J. Huthnance, and R. Williams, 2013: Internal wave reflection on shelf-slopes with depth-  
 947 varying stratification. *Journal of Physical Oceanography*, **43**, 243–258.

948 Harrison, M., and R. Hallberg, 2008: Pacific subtropical cell response to reduced equatorial dissi-  
 949 pation. *Journal of Physical Oceanography*, **38**, 1894–1912.

950 Hazewinkel, J., and K. B. Winters, 2011: PSI of the internal tide on a  $\beta$ -plane: Flux divergence  
 951 and near-inertial wave propagation. *Journal of Physical Oceanography*, **41**, 1673–1682.

952 Helfrich, K. R., and R. H. J. Grimshaw, 2008: Nonlinear disintegration of the internal tide. *Journal*  
 953 *of Physical Oceanography*, **38**, 686–701.

954 Henyey, F., and N. Pomphrey, 1983: Eikonal description of internal wave interactions: A non-  
 955 diffusive picture of “induced diffusion”. *Dynamics of Atmospheres and Oceans*, **7**, 189–219.

956 Henyey, F. S., J. Wright, and S. M. Flatté, 1986: Energy and action flow through the internal wave  
 957 field. *J. Geophys. Res.*, **91 (C7)**, 8487–8495.

958 Huussen, T. N., A. C. Naveira-Garabato, H. L. Bryden, and E. L. McDonagh, 2012: Is the deep  
 959 Indian Ocean MOC sustained by breaking internal waves? *J. Geophys. Res.*, **117 (C8)**, C08 024.

960 Ilıcak, M., A. Adcroft, S. Griffies, and R. Hallberg, 2012: Spurious dianeutral mixing and the role  
 961 of momentum closure. *Ocean Modelling*, **45–46**, 37–58.

- Ivey, G., and R. Nokes, 1989: Vertical mixing due to the breaking of critical internal waves on sloping boundaries. *Journal of Fluid Mechanics*, **204**, 479–500.
- Ivey, G., K. Winters, and I. de Silva, 2000: Turbulent mixing in a sloping benthic boundary layer energized by internal waves. *Journal of Fluid Mechanics*, **418**, 59–76.
- Ivey, G., K. Winters, and J. Koseff, 2008: Density stratification, turbulence, but how much mixing? *Ann. Rev. Fluid Mech.*, **40**, 169–184.
- Jackson, L., R. Hallberg, and S. Legg, 2008: A Parameterization of Shear-Driven Turbulence for Ocean Climate Models. *Journal of Physical Oceanography*, **38**, 1033–1053.
- Jayne, S. R., 2009: The impact of abyssal mixing parameterizations in an ocean general circulation model. *Journal of Physical Oceanography*, **39**, 1756—1775.
- Jayne, S. R., and L. C. St. Laurent, 2001: Parameterizing tidal dissipation over rough topography. *Geophys. Res. Lett.*, **28** (5), 811–814.
- Jochum, M., 2009: Impact of latitudinal variations in vertical diffusivity on climate simulations. *Journal of Geophysical Research*, **114**, C01010, doi:10.1029/2008JC005030.
- Jochum, M., B. P. Briegleb, G. Danabasoglu, W. G. Large, N. J. Norton, S. R. Jayne, M. H. Alford, and F. O. Bryan, 2013: The impact of oceanic near-inertial waves on climate. *J. Climate*, **26** (9), 2833–2844, doi:10.1175/JCLI-D-12-00181.1.
- Johnston, T. M. S., and M. A. Merrifield, 2003: Internal tide scattering at seamounts, ridges and islands. *Journal of Geophysical Research*, **108**(C6), doi:10.1029/2002JC001528.
- Johnston, T. M. S., D. L. Rudnick, and S. M. Kelly, 2015: Standing internal tides in the Tasman Sea observed by gliders. *Journal of Physical Oceanography*, **45**, doi:10.1175/JPO-D-15-0038.1.

- 983 Kelly, S. M., N. L. Jones, J. D. Nash, and A. F. Waterhouse, 2013: The geography of semidiurnal  
984 mode-1 internal-tide energy loss. *Geophysical Research Letters*, **40**, 4689–4693, doi:10.1002/  
985 grl.50872.
- 986 Kelly, S. M., J. D. Nash, K. I. Martini, M. H. Alford, and E. Kunze, 2012: The cascade of tidal  
987 energy from low to high modes on a continental slope. *Journal of Physical Oceanography*, **42**,  
988 doi:10.1175/JPO-11-0231.1.
- 989 Kerry, C., B. Powell, and G. Carter, 2014: The impact of subtidal circulation on internal-tide-  
990 induced mixing in the Philippine sea. *Journal of Physical Oceanography*, **44**, 3209–3224, doi:  
991 10.1175/JPO-D-13-0142.1.
- 992 Klinger, B. A., J. Marshall, and U. Send, 1996: Representation of convective plumes by vertical  
993 adjustment. *Journal of Geophysical Research*, **101**, 18 175–18 182.
- 994 Klymak, J., M. Buijsman, S. Legg, and R. Pinkel, 2013: Parameterizing surface and internal tide  
995 scattering and breaking on supercritical topography: the one- and two-ridge cases. *Journal of*  
996 *Physical Oceanography*, **43**, 1380–1397.
- 997 Klymak, J. M., M. H. Alford, R. Pinkel, R. C. Lien, and Y. J. Yang, 2011: The breaking and  
998 scattering of the internal tide on a continental slope. *Journal of Physical Oceanography*, **41** (5),  
999 926–945, doi:10.1175/2010JPO4500.1.
- 1000 Klymak, J. M., S. Legg, and R. Pinkel, 2010: A simple parameterization of turbulent tidal mixing  
1001 near supercritical topography. *Journal of Physical Oceanography*, **40** (9), 2059–2074, doi:10.  
1002 1175/2010JPO4396.1, <http://journals.ametsoc.org/doi/pdf/10.1175/2010JPO4396.1>.
- 1003 Klymak, J. M., R. Pinkel, and L. Rainville, 2008: Direct breaking of the internal tide near topog-  
1004 raphy: Kaena Ridge, Hawaii. *Journal of Physical Oceanography*, **38**, 380–399.

1005 Klymak, J. M., and Coauthors, 2006: An estimate of tidal energy lost to turbulence at the Hawaiian  
 1006 Ridge. *Journal of Physical Oceanography*, **36** (6), 1148–1164.

1007 Kunze, E., 2017: Internal-wave-driven mixing: Geography and budgets. *J. Phys. Oceanogr.*, (**in**  
 1008 **review**).

1009 Kunze, E., E. Firing, J. Hummon, T. K. Chereskin, and A. Thurnherr, 2006: Global abyssal mixing  
 1010 inferred from lowered ADCP shear and CTD strain profiles. *Journal of Physical Oceanography*,  
 1011 **36**, 1553–1576.

1012 Kunze, E., C. MacKay, E. E. McPhee-Shaw, K. Morrice, J. B. Girton, and S. R. Terker, 2012:  
 1013 Turbulent mixing and exchange with interior waters on sloping boundaries. *Journal of Physical*  
 1014 *Oceanography*, **42**, 910–927.

1015 Kunze, E., R. W. Schmitt, and J. M. Toole, 1995: The energy balance in a warm-core ring's  
 1016 near-inertial critical layer. *Journal of Physical Oceanography*, **25** (5), 942–957.

1017 Large, W., and G. Crawford, 1995: Observations and simulations of upper-ocean response to wind  
 1018 events during the ocean storms experiment. *Journal of physical Oceanography*, **25** (11), 2831–  
 1019 2852.

1020 Large, W., J. McWilliams, and S. Doney, 1994: Oceanic vertical mixing: a review and a model  
 1021 with a nonlocal boundary layer parameterization. *Reviews of Geophysics*, **32**, 363–403.

1022 Lefauve, A., C. Muller, and A. Melet, 2015: A three-dimensional map of tidal dissipation over  
 1023 abyssal hills. *Journal of Geophysical Research: Oceans*, **120** (7), 4760–4777.

1024 Legg, S., 2014: Scattering of low-mode internal waves at finite isolated topography. *Journal of*  
 1025 *Physical Oceanography*, **44** (1), 359–383, doi:10.1175/JPO-D-12-0241.1.

- 1026 Legg, S., and A. Adcroft, 2003: Internal wave breaking at concave and convex continental slopes.  
1027 *Journal of Physical Oceanography*, **33**, 2224–2246.
- 1028 Legg, S., R. Hallberg, and J. Girton, 2006: Comparison of entrainment in overflows simulated by  
1029 z-coordinate, isopycnal and non-hydrostatic models. *Ocean Modelling*, **11**, 69–97.
- 1030 Legg, S., and J. M. Klymak, 2008: Internal hydraulic jumps and overturning generated by tidal  
1031 flow over a steep ridge. *Journal of Physical Oceanography*, **38**, 1949–1964.
- 1032 Lighthill, J., 1976: *Waves in fluids*. Cambridge University Press.
- 1033 Llewellyn Smith, S. G., and W. R. Young, 2003: Tidal conversion at a very steep ridge. *J. Fluid*  
1034 *Mech.*, **495**, 175–191.
- 1035 Lumpkin, R., and K. Speer, 2007: Global ocean meridional overturning. *Journal of Physical*  
1036 *Oceanography*, **37**, 2550–2562.
- 1037 Lvov, Y., K. L. Polzin, and E. G. Tabak, 2004: Energy spectra of the ocean’s internal wave field:  
1038 Theory and observations. *Phys. Rev. Lett.*, **92** (12), 128 501–1–128 501–4.
- 1039 MacKinnon, J., 2013: Mountain waves in the deep ocean. *Nature*, **501** (7467), 321–322.
- 1040 MacKinnon, J., Louis St. Laurent, and A. N. Garabato, 2013a: Diapycnal mixing processes in  
1041 the ocean interior. *Ocean Circulation and Climate, 2nd Edition: A 21st century perspective*,  
1042 G. Siedler, S. M. Griffies, J. Gould, and J. Church, Eds., International Geophysics Series, Vol.  
1043 103, Academic Press, 159–183.
- 1044 MacKinnon, J., and K. Winters, 2003: Spectral evolution of bottom-forced internal waves.  
1045 *Near-Boundary Processes and Their Parameterization, Proceedings of the 13th ‘Aha Huliko’a*  
1046 *Hawaiian Winter Workshop*, P. Muller, and D. Henderson, Eds., 73–83.

- 1047 MacKinnon, J., and K. Winters, 2005: Subtropical catastrophe: significant loss of low-mode tidal  
1048 energy at 28.9. *Geophys. Res. Lett.*, **32**, 1–5.
- 1049 MacKinnon, J. A., M. H. Alford, R. Pinkel, J. Klymak, and Z. Zhao, 2013b: The latitudinal  
1050 dependence of shear and mixing in the Pacific transiting the critical latitude for PSI. *Journal of*  
1051 *Physical Oceanography*, **43** (1), 3–16.
- 1052 MacKinnon, J. A., M. H. Alford, O. Sun, R. Pinkel, Z. Zhao, and J. Klymak, 2013c: Parametric  
1053 subharmonic instability of the internal tide at 29N. *Journal of Physical Oceanography*, **43**, 17–  
1054 28, doi:10.1175/JPO-D-11-0108.1.
- 1055 Mackinnon, J. A., and M. C. Gregg, 2003: Shear and Baroclinic Energy Flux on the Summer New  
1056 England Shelf. *Journal of Physical Oceanography*, **33**, 1462–1475.
- 1057 Martini, K. I., M. H. Alford, E. Kunze, S. M. Kelly, and J. D. Nash, 2011: Observations of internal  
1058 tides on the Oregon continental slope. *Journal of Physical Oceanography*, **41**, 1772–1794.
- 1059 Martini, K. I., M. H. Alford, E. Kunze, S. M. Kelly, and J. D. Nash, 2013: Internal Bores and  
1060 Breaking Internal Tides on the Oregon Continental Slope. *Journal of Physical Oceanography*,  
1061 **43** (1), 120–139.
- 1062 Mashayek, A., C. Caulfield, and W. Peltier, 2013: Time-dependent, non-monotonic mixing in  
1063 stratified turbulent shear flows: implications for oceanographic estimates of buoyancy flux.  
1064 *Journal of Fluid Mechanics*, **736**, 570–593.
- 1065 Mathur, M., G. S. Carter, and T. Peacock, 2014: Topographic scattering of the low-mode internal  
1066 tide in the deep ocean. *Journal of Geophysical Research: Oceans*, **119**, 2165–2182, doi:10.  
1067 1002/2013JC009152.

- 1068 McComas, C. H., 1977: Equilibrium mechanisms within the oceanic internal wave field. *Journal*  
1069 *of Physical Oceanography*, **7**, 836–845.
- 1070 Melet, A., R. Hallberg, A. Adcroft, M. Nikurashin, and S. Legg, 2015: Energy flux into internal  
1071 lee waves: sensitivity to future climate changes using linear theory and a climate model. *Journal*  
1072 *of Climate*, **28**, 2365–2384.
- 1073 Melet, A., R. Hallberg, S. Legg, and M. Nikurashin, 2014: Sensitivity of the ocean state to  
1074 lee wave–driven mixing. *Journal of Physical Oceanography*, **44** (3), 900–921, doi:10.1175/  
1075 JPO-D-13-072.1.
- 1076 Melet, A., R. Hallberg, S. Legg, and K. L. Polzin, 2013a: Sensitivity of the ocean state to the  
1077 vertical distribution of internal-tide-driven mixing. *Journal of Physical Oceanography*, **43** (3),  
1078 602–615, doi:http://dx.doi.org/10.1175/JPO-D-12-055.1.
- 1079 Melet, A., S. Legg, and R. Hallberg, 2016: Climatic impacts of parameterized local and remote  
1080 tidal mixing. *Journal of Climate*, **29** (10), 3473–3500.
- 1081 Melet, A., M. Nikurashin, C. J. Muller, S. Falahat, J. Nycander, P. G. Timko, B. K. Arbic, and  
1082 J. A. Goff, 2013b: Internal tide generation by abyssal hills using analytical theory. *Journal of*  
1083 *Geophysical Research - Oceans*, **118**, 6303–6318.
- 1084 Moum, J. N., K. Pujiana, R.-C. Lien, and W. D. Smyth, 2016: Ocean feedback to pulses of the  
1085 madden–julian oscillation in the equatorial indian ocean. *Nature communications*, **7**.
- 1086 Muller, C. J., and O. Bühler, 2009: Saturation of the internal tides and induced mixing in the  
1087 abyssal ocean. *Journal of Physical Oceanography*, **39**, 2077–2096.

- Müller, M., B. K. Arbic, J. G. Richman, J. F. Shriver, E. L. Kunze, R. B. Scott, A. J. Wallcraft, and L. Zamudio, 2015: Toward an internal gravity wave spectrum in global ocean models. *Geophysical Research Letters*, **42** (9), 3474–3481.
- Müller, M., J. Cherniawsky, M. Foreman, and J.-S. von Storch, 2012: Global map of  $M_2$  internal tide and its seasonal variability from high resolution ocean circulation and tide modelling. *Geophysical Research Letters*, **39**, L19607, doi:10.1029/2012GL053320.
- Müller, P., G. Holloway, F. Henyey, and N. Pomphrey, 1986: Nonlinear interactions among internal gravity waves. *Rev. Geophys*, **24** (3), 493–536.
- Müller, P., and A. Natarov, 2003: The internal wave action model (iwam). *Near-Boundary Processes and Their Parameterization: Proc. 'Aha Huliko'a Winter Workshop*, Citeseer, 95–105.
- Musgrave, R., R. Pinkel, J. MacKinnon, M. R. Mazloff, and W. Young, 2016: Stratified tidal flow over a tall ridge above and below the turning latitude. *Journal of Fluid Mechanics*, **793**, 933–957.
- Nagai, T., and T. Hibiya, 2015: Internal tides and associated vertical mixing in the Indonesian archipelago. *Journal of Geophysical Research: Oceans*, **120** (5), 3373–3390.
- Nash, J. D., M. H. Alford, E. Kunze, K. I. Martini, and S. Kelly, 2007: Hotspots of deep ocean mixing on the Oregon continental slope. *Geophys. Res. Lett.*, **34** (L01605), doi:10.1029/2006GL028170.
- Nash, J. D., E. Kunze, J. M. Toole, and R. W. Schmitt, 2004: Internal tide reflection and turbulent mixing on the continental slope. *Journal of Physical Oceanography*, **34**, 1117–1134.
- Naveira Garabato, A. C., K. L. Polzin, B. A. King, K. J. Heywood, and M. Visbeck, 2004: Widespread intense turbulent mixing in the Southern Ocean. *Science*, **303**, 210–213.



1110 Nikurashin, M., and R. Ferrari, 2011: Global energy conversion rate from geostrophic  
 1111 flows into internal lee waves in the deep ocean. *Geophys. Res. Lett.*, **38** (L08610),  
 1112 doi:10.1029/2011GL046576.

1113 Nikurashin, M., and R. Ferrari, 2013: Overturning circulation driven by breaking internal waves  
 1114 in the deep ocean. *Geophys. Res. Lett.*, **40** (12), 3133–3137, doi:10.1002/grl.50542.

1115 Nikurashin, M., R. Ferrari, N. Grisouard, and K. Polzin, 2014: The impact of finite amplitude  
 1116 bottom topography on internal wave generation in the Southern Ocean. *Journal of Physical*  
 1117 *Oceanography*, **44**, 2938–2950.

1118 Nikurashin, M., and S. Legg, 2011: A mechanism for local dissipation of internal tides generated  
 1119 at rough topography. *Journal of Physical Oceanography*, **41**, 378–395.

1120 Niwa, Y., and T. Hibiya, 2011: Estimation of baroclinic tide energy available for deep ocean  
 1121 mixing based on three-dimensional global numerical simulations. *Journal of Oceanography*,  
 1122 **67** (4), 493–502.

1123 Niwa, Y., and T. Hibiya, 2014: Generation of baroclinic tide energy in a global three-dimensional  
 1124 numerical model with different spatial grid resolutions. *Ocean Modelling*, **80**, 59–73.

1125 Osborn, T. R., 1980: Estimates of the local rate of vertical diffusion from dissipation measure-  
 1126 ments. *Journal of Physical Oceanography*, **10**, 83–89.

1127 Pacanowski, R. C., and G. Philander, 1981: Parameterization of vertical mixing in numerical  
 1128 models of the tropical ocean. *Journal of Physical Oceanography*, **11**, 1442–1451.

1129 Palmer, W. R., G. J. Shutts, and R. Swinbank, 1986: Alleviation of systematic westerly bias  
 1130 in general circulation and numerical weather prediction models through an orographic gravity

1131 wave drag parameterization. *Quarterly Journal of the Royal Meteorological Society*, **112**(474),  
 1132 1001–1039.

1133 Peltier, W. R., and C. P. Caulfield, 2003: Mixing efficiency in stratified shear flows. *Annual Review*  
 1134 *of Fluid Mechanics*, **35** (1), 135–167, doi:10.1146/annurev.fluid.35.101101.161144.

1135 Pierrehumbert, R., and J. Bacmeister, 1987: On the realizability of long’s model solutions for  
 1136 nonlinear stratified flow over an obstacle. *Stratified Flows*, ASCE, 99–112.

1137 Pinkel, R., and Coauthors, 2015: Breaking internal tides keep the ocean in balance. *EOS Transac-*  
 1138 *tions*, **96**.

1139 Plueddemann, A. J., and J. T. Farrar, 2006: Observations and models of the energy flux from the  
 1140 wind to mixed layer inertial currents. *Deep-Sea Research*, **53**, 5–30.

1141 Polzin, K. L., 2004a: A flux representation of internal wave spectral transports. *Journal of Physical*  
 1142 *Oceanography*, **34**, 214–230.

1143 Polzin, K. L., 2004b: Idealized solutions for the energy balance of the finescale internal wave field.  
 1144 *Journal of Physical Oceanography*, **34** (1), 231–246.

1145 Polzin, K. L., 2009: An abyssal recipe. *Ocean Modelling*, **30**, 298–309.

1146 Polzin, K. L., 2010: Mesoscale Eddy-Internal Wave Coupling. Part II: Energetics and Results from  
 1147 PolyMode. *Journal of Physical Oceanography*, **40** (4), 789–801.

1148 Polzin, K. L., A. C. Naveira Garabato, T. N. Huussen, B. M. Sloyan, and S. Waterman, 2014:  
 1149 Finescale parameterizations of turbulent dissipation. *Journal of Geophysical Research: Oceans*,  
 1150 **119** (2), 1383–1419.

1151 Polzin, K. L., N. S. Oakey, J. M. Toole, and R. W. Schmitt, 1996: Fine structure and microstructure  
 1152 characteristics across the northwest Atlantic Subtropical Front. *J. Geophys. Res.*, **101 (C6)**,  
 1153 14 111–14 121.

1154 Polzin, K. L., J. M. Toole, J. R. Ledwell, and R. W. Schmitt, 1997: Spatial variability of turbulent  
 1155 mixing in the abyssal ocean. *Science*, **276**, 93–96.

1156 Polzin, K. L., J. M. Toole, and R. W. Schmitt, 1995: Finescale parameterizations of turbulent  
 1157 dissipation. *Journal of Physical Oceanography*, **25**, 306–328.

1158 Rahmstorf, S., 1993: A fast and complete convection scheme for ocean models. *Ocean Modelling*,  
 1159 **101**, 9–11.

1160 Rainville, L., and R. Pinkel, 2006: Baroclinic energy flux at the Hawaiian Ridge: Observations  
 1161 from the R/P FLIP. *Journal of Physical Oceanography*, **36 (6)**, 1104–1122.

1162 Ray, R. D., and G. T. Mitchum, 1996: Surface manifestation of internal tides generated near  
 1163 Hawaii. *Geophys. Res. Lett.*, **23 (16)**, 2101–2104.

1164 Rimac, A., J.-S. v. Storch, and C. Eden, 2016: The total energy flux leaving the ocean’s mixed  
 1165 layer. *Journal of Physical Oceanography*, **46 (6)**, 1885–1900.

1166 Rimac, A., J.-S. von Storch, C. Eden, and H. Haak, 2013: The influence of high-resolution wind  
 1167 stress field on the power input to near-inertial motions in the ocean. *Geophysical Research*  
 1168 *Letters*, **40 (18)**, 4882–4886, doi:10.1002/grl.50929.

1169 Rocha, C. B., T. K. Chereskin, S. T. Gille, and D. Menemenlis, 2016: Mesoscale to submesoscale  
 1170 wavenumber spectra in drake passage. *Journal of Physical Oceanography*, **46 (2)**, 601–620,  
 1171 doi:10.1175/JPO-D-15-0087.1.

1172 Rudnick, D., and Coauthors, 2003: From tides to mixing along the Hawaiian Ridge. *Science*, **301**,  
1173 355–357.

1174 Salehipour, H., W. R. Peltier, C. B. Whalen, and J. A. Mackinnon, 2016: A new characterization of  
1175 the turbulent diapycnal diffusivities of mass and momentum in the ocean. *Geophysical Research*  
1176 *Letters*, n/a–n/a.

1177 Schmitt, R. W., J. R. Ledwell, E. T. Montgomery, K. L. Polzin, and J. M. Toole, 2005: Enhanced  
1178 diapycnal mixing by salt fingers in the thermocline of the tropical Atlantic. *Science*, **308**, 685–  
1179 688.

1180 Schmittner, A., and G. Egbert, 2014: An improved parameterization of tidal mixing for ocean  
1181 models. *Geosci. Model Dev.*, **7**, 211–224.

1182 Scott, R., J. Goff, A. Garabato, and A. Nurser, 2011: Global rate and spectral characteristics of  
1183 internal gravity wave generation by geostrophic flow over topography. *Journal of Geophysical*  
1184 *Research*, **116 (C9)**, C09 029.

1185 Sheen, K., and Coauthors, 2014: Eddy-induced variability in southern ocean abyssal mixing on  
1186 climatic timescales. *Nature Geoscience*, **7(8)**, 577–582.

1187 Sheen, K. L., and Coauthors, 2013: Rates and mechanisms of turbulent dissipation and mixing  
1188 in the Southern Ocean: Results from the Diapycnal and Isopycnal Mixing Experiment in the  
1189 Southern Ocean (DIMES). *J. Geophys. Res.*, **118**, 1–19, doi:http://10.1002/jgrc.20217.

1190 Shriver, J., B. K. Arbic, J. Richman, R. Ray, E. Metzger, A. Wallcraft, and P. Timko, 2012:  
1191 An evaluation of the barotropic and internal tides in a high-resolution global ocean circulation  
1192 model. *Journal of Geophysical Research: Oceans (1978–2012)*, **117 (C10)**.

Shriver, J., J. Richman, and B. Arbic, 2014: How stationary are the internal tides in a high-resolution global ocean circulation model? *Journal of Geophysical Research: Oceans*, **119**, 2769–2787, doi:10.1002/2013JC009423.

Silverthorne, K. E., and J. M. Toole, 2009: Seasonal kinetic energy variability of near-inertial motions. *Journal of Physical Oceanography*, **39** (4), 1035–1049.

Simmons, H. L., 2008: Spectral modification and geographic redistribution of the semi-diurnal internal tide. *Ocean Modelling*, **21**, 126–138.

Simmons, H. L., and M. H. Alford, 2012: Simulating the long range swell of internal waves generated by ocean storms. *Oceanography*, **25** (2), 30–41.

Simmons, H. L., R. W. Hallberg, and B. K. Arbic, 2004a: Internal wave generation in a global baroclinic tide model. *Deep-Sea Res II*, **51**, 3043–3068.

Simmons, H. L., S. R. Jayne, L. C. St. Laurent, and A. J. Weaver, 2004b: Tidally driven mixing in a numerical model of the ocean general circulation. *Ocean Modelling*, **6**, 245–263.

Slinn, D. N., and J. J. Riley, 1996: Turbulent mixing in the oceanic boundary layer caused by internal wave reflection from sloping terrain. *Dynamics of atmospheres and oceans*, **24** (1), 51–62.

St. Laurent, L., and C. Garrett, 2002: The role of internal tides in mixing the deep ocean. *Journal of Physical Oceanography*, **32** (10), 2882–2899.

St. Laurent, L., H. Simmons, and S. Jayne, 2002: Estimating tidally driven mixing in the deep ocean. *Geophys. Res. Lett.*, **29** (23).

St. Laurent, L. C., 2008: Turbulent dissipation on the margins of the South China Sea. *Geophys. Res. Lett.*, **35** (L23615), doi:10.1029/2008GL035520.

- 1215 St. Laurent, L. C., and J. D. Nash, 2004: An examination of the radiative and dissipative properties  
1216 of deep ocean internal tides. *Deep-Sea Research II*, **51**, 3029–3042.
- 1217 St. Laurent, L. C., A. C. Naveira Garabato, J. R. Ledwell, A. M. Thurnherr, J. M. Toole, and  
1218 A. J. Watson, 2012: Turbulence and diapycnal mixing in Drake Passage. *Journal of Physical*  
1219 *Oceanography*, **42**, 2143–2152.
- 1220 St. Laurent, L. C., and H. L. Simmons, 2006: Estimates of power consumed by mixing in the  
1221 ocean interior. *Journal of Climate*, **19**, 4877–4890.
- 1222 Staquet, C., and J. Sommeria, 2002: Internal gravity waves: From instability to turbulence. *Annual*  
1223 *Reviews of Fluid Mechanics*, **34**, 559–593.
- 1224 Sun, O. M., and R. Pinkel, 2012: Energy transfer from high-shear, low-frequency internal waves  
1225 to high-frequency waves near Kaena Ridge, Hawai'i. *Journal of Physical Oceanography*, **42**,  
1226 doi:10.1175/JPO-D-11-0117.1.
- 1227 Sun, O. M., and R. Pinkel, 2013: Subharmonic energy transfer from the semidiurnal internal tide  
1228 to near-diurnal motions over Kaena Ridge, Hawai'i. *Journal of Physical Oceanography*, doi:  
1229 10.1175/JPO-D-12-0141.1.
- 1230 Tanaka, T., I. Yasuda, Y. Tanaka, and G. S. Carter, 2013: Numerical study on tidal mixing along the  
1231 shelf break in the Green Belt in the southeastern Bering Sea. *Journal of Geophysical Research:*  
1232 *Oceans*, **118**, 6525–6542.
- 1233 Thoppil, P., J. Richman, and P. Hogan, 2011: Energetics of a global ocean circulation model  
1234 compared to observations. *Geophysical Research Letters*, **38**, L15 607.

1235 Thurnherr, A. M., L. C. St. Laurent, K. G. Speer, J. M. Toole, and J. R. Ledwell, 2005: Mixing as-  
 1236 sociated with sills in a canyon on the midocean ridge flank. *Journal of Physical Oceanography*,  
 1237 **35**, 1370–1381.

1238 Trossman, D. S., B. K. Arbic, S. T. Garner, J. A. Goff, S. R. Jayne, E. J. Metzger, and A. J.  
 1239 Wallcraft, 2013: Impact of parameterized lee wave drag on the energy budget of an eddying  
 1240 global ocean model. *Ocean Modelling*, **72**, 119–142.

1241 Trossman, D. S., B. K. Arbic, J. G. Richman, S. T. Garner, S. R. Jayne, and A. J. Wallcraft, 2016:  
 1242 Impact of Topographic Internal Lee Wave Drag on an Eddying Global Ocean Model. *Ocean*  
 1243 *Modelling*, **97**, 109–128.

1244 Trossman, D. S., S. Waterman, K. L. Polzin, B. K. Arbic, S. T. Garner, A. C. Naveira-Garabato,  
 1245 and K. L. Sheen, 2015: Internal Lee Wave Closures: Parameter Sensitivity and Comparison to  
 1246 Observations. *Journal of Geophysical Research-Oceans*, **120**, 7997–8019.

1247 Venayagamoorthy, S., and O. Fringer, 2006: Numerical simulations of the interaction of internal  
 1248 waves with a shelf-break. *Physics of Fluids*, **18**, 076 603.

1249 Venayagamoorthy, S. K., and J. R. Koseff, 2016: On the flux richardson number in stably stratified  
 1250 turbulence. *Journal of Fluid Mechanics*, **798**, R1.

1251 Wain, D. J., M. C. Gregg, M. H. Alford, R. C. Lien, G. S. Carter, and R. A. Hall, 2013: Propagation  
 1252 and dissipation of the internal tide in upper Monterey Canyon. *J. Geophys. Res.*, **118**, 4855–  
 1253 4877.

1254 WAMDI-Group, 1988: The WAM model-a third generation ocean wave prediction model. *Journal*  
 1255 *of Physical Oceanography*, **18 (12)**, 1775–1810.

- 1256 Waterhouse, A. F., J. A. MacKinnon, R. C. Musgrave, S. M. Kelly, A. I. Pickering, and J. Nash,  
1257 2017: Internal tide convergence and mixing in a submarine canyon. *Journal of Physical*  
1258 *Oceanography*, **47** (2), 303–322.
- 1259 Waterhouse, A. F., and Coauthors, 2014: Global patterns of diapycnal mixing from measurements  
1260 of the turbulent dissipation rate. *Journal of Physical Oceanography*, **44** (7), 1854–1872.
- 1261 Waterman, S., A. C. Naveira Garabato, and K. L. Polzin, 2013: Internal waves and turbulence in  
1262 the Antarctic Circumpolar Current. *Journal of Physical Oceanography*, **43**, 259–282.
- 1263 Waterman, S., K. L. Polzin, A. C. Naveira Garabato, K. L. Sheen, and A. Forryan, 2014: Suppres-  
1264 sion of internal wave breaking in the Antarctic Circumpolar Current near topography. *Journal*  
1265 *of Physical Oceanography*, **44** (5), 1466–1492.
- 1266 Whalen, C. B., 2015: Illuminating spatial and temporal patterns of ocean mixing as inferred from  
1267 argo profiling floats. Ph.D. thesis, UNIVERSITY OF CALIFORNIA, SAN DIEGO.
- 1268 Whalen, C. B., J. A. MacKinnon, L. D. Talley, and A. F. Waterhouse, 2015: Estimating the mean  
1269 diapycnal mixing using a finescale strain parameterization. *Journal of Physical Oceanography*,  
1270 **45** (4), 1174.
- 1271 Whalen, C. B., L. D. Talley, and J. A. MacKinnon, 2012: Spatial and temporal variabil-  
1272 ity of global ocean mixing inferred from argo profiles. *Geophys. Res. Lett.*, **39** (L18612),  
1273 doi:10.1029/2012GL053196.
- 1274 Wijesekera, H. W., L. Padman, T. Dillon, M. Levine, C. Paulson, and R. Pinkel, 1993: The ap-  
1275 plication of internal-wave dissipation models to a region of strong mixing. *Journal of Physical*  
1276 *Oceanography*, **23**, 269–286.



- 1277 Winkel, D. P., M. C. Gregg, and T. B. Sanford, 2002: Patterns of Shear and Turbulence across the  
1278 Florida Current. *Journal of Physical Oceanography*, **32**, 3269–3285.
- 1279 Wright, C. J., R. B. Scott, P. Ailliot, and D. Furnival, 2014: Lee wave generation rates in the deep  
1280 ocean. *Geophysical Research Letters*, **41**, doi:10.1002/2013GL059087.
- 1281 Wu, L., Z. Jing, S. Riser, and M. Visbeck, 2011: Seasonal and spatial variations of Southern Ocean  
1282 diapycnal mixing from Argo profiling floats. *Nature Geoscience*, **4** (6), 363–366.
- 1283 Wunsch, C., 1969: Progressive internal waves on slopes. *Journal of Fluid Mechanics*, **35**, 131–  
1284 145.
- 1285 Zhang, L., and H. L. Swinney, 2014: Virtual seafloor reduces internal wave generation by tidal  
1286 flow. *Phys. Rev. Lett.*, **112**, 14502.
- 1287 Zhao, Z., M. H. Alford, J. B. Girton, L. Rainville, and H. L. Simmons, 2016: Global observations  
1288 of open-ocean mode-1  $M_2$  internal tides. *Journal of Physical Oceanography*, **46**, 1657–1684,  
1289 doi:10.1175/JPO-D-15-0105.1.
- 1290 Zhao, Z., M. H. Alford, J. A. MacKinnon, and R. Pinkel, 2010: Long-range propagation of the  
1291 semidiurnal internal tide from the Hawaiian Ridge. *Journal of Physical Oceanography*, **40** (4),  
1292 713–736, doi:10.1175/2009JPO4207.1.

## LIST OF FIGURES

- Fig. 1.** Schematic of internal wave mixing processes in the open ocean that are considered as part of this CPT. Tides interact with topographic features to generate high-mode internal waves (e.g. at mid-ocean ridges) and low-mode internal waves (e.g. at tall steep ridges such as the Hawaiian Ridge). Deep currents flowing over topography can generate lee waves (e.g. in the Southern Ocean). Storms cause inertial oscillations in the mixed layer, which can generate both low and high mode internal waves (e.g. beneath storm tracks). In the open ocean these internal waves can scatter off of rough topography and potentially interact with mesoscale fronts and eddies, until they ultimately dissipate through wave-wave interactions. Internal waves that reach the shelf and slope can scatter, or amplify as propagate towards shallower water. . . . . 61
- Fig. 2.** Depth-averaged diffusivity  $\kappa$  from (a) the upper ocean (from MLD to 1000 m depth) and (b) the full water column, updated from (Waterhouse et al. 2014). The background diffusivity map in (a) comes from the strain-based inferences of diffusivity from Argo floats, updated from (Whalen et al. 2015) with observations included from 2006–2015. (c) Compiled observations of mixing measurements with blue and green squares and diamonds denoting microstructure measurements. Green represents full-depth profiles, while blue denotes microstructure profiles. Purple circles represent inferred diffusivity from a finescale parameterization using LADCP/CTD profiles [dark purple, Kunze et al. (2006); medium purple, Huussen et al. (2012)] and HDSS shipboard shear (light orange). Dark orange circles are diffusivities from density overturns in moored profiles. . . . . 62
- Fig. 3.** a) A snapshot of baroclinic velocity (m/s) from a two-dimensional numerical simulation of internal tides forced by  $M_2$  (semi-diurnal) tidal velocities over rough topography, for parameters corresponding to the Brazil Basin (Nikurashin and Legg 2011); (b) observational time series of internal wave breaking over tall steep topography; here we see northward velocity (upper) and turbulent dissipation rate (lower) oscillate twice a day as the tide flows over Kaena Ridge, Hawaii (Klymak et al. 2008) (c) global energy flux from the  $M_2$  tide into internal tides (in  $\log_{10} W/m^2$ ) estimated using (top) the topography resolved in the SRTM30.PLUS bathymetry data base and (bottom) a statistical representation of unresolved abyssal hill topography estimates (Melet et al. 2013b); (d) the vertical structure of dissipation from Brazil Basin observations (thick solid curve) and the Polzin 2009 (Eqn. 4) parameterization of nearfield internal tide dissipation (thin solid curve); (e) the impact of the Polzin parameterization in the GFDL CM2G coupled climate model: (top) The Indo-Pacific meridional overturning streamfunction ( $S_v$ )(averaged over the final 100 years of a 1000 year simulation) using the Polzin (2009) parameterization, (bottom) the differences in Indo-Pacific meridional overturning streamfunction ( $S_v$ ) between the simulations with the Polzin (2009) parameterization and the St. Laurent et al. (2002) parameterization as implemented by Simmons et al. (2004b) (from Melet et al. (2013a)). . . . . 63
- Fig. 4.** Farfield internal tide: (a) SSH amplitude (unit: mm) of global mode-1  $M_2$  internal tides from multisatellite altimetry (Zhao et al. 2016). The light blue color indicates regions of high mesoscale activity, which make extraction of internal tides from altimetry difficult. (b)-(c) Modeled semidiurnal tidal fluxes and comparison to observations: (b) HYCOM modeled semidiurnal internal tide barotropic-to-baroclinic conversion rates (background color) and vertically-integrated energy flux vectors (black arrows, plotted every 768th grid point for clarity), and (c) depth-integrated semidiurnal mode-1 energy fluxes in HYCOM (red arrows) and high-resolution mooring observations to the north of Hawaii (blue arrows) (Ansong et al. 2017). (d)-(f) Impact on thermosteric sea level of using different spatial distribution of remote internal tide energy dissipation in GFDL ESM2G climate model: (d) thermosteric sea level (unit: m) in a reference simulation using a constant background diapycnal diffusivity

for remote internal tide dissipation. Anomalies (in m) of thermosteric sea level from the reference case in (d) for simulations where (e) all internal tide energy is dissipated locally, over the generation site, (f) 20 % of the internal tide energy is dissipated locally and 80 % is dissipated uniformly over the ocean basins with a vertical profile proportional to buoyancy squared  $N^2$  (Melet et al. 2016). . . . . 64

**Fig. 5.** Internal lee waves: a) observations from DIMES showing (left) turbulent dissipation rates (in logarithmic scales from  $10^{-10}$  to  $10^{-7}$  W kg $^{-1}$ ) for the Phoenix Ridge (circles in right inset), and (middle) average height above bottom profiles of turbulent kinetic energy dissipation (see details in St. Laurent et al. (2012)), b) power conversion into lee waves (Nikurashin and Ferrari (2011) used in Melet et al. (2014)), c) consequences of parameterized lee wave mixing on the global ocean meridional overturning circulation ( $S_v$ , averaged over the final 100 years of 1000 years simulations, from Melet et al. (2014)) , d) global map of depth-integrated dissipation due to parameterized topographic wave drag inserted inline into global 1/25° HYCOM simulation, from Trossman et al. (2016). . . . . 65

**Fig. 6.** Near-inertial internal waves: a) observational example from Alford et al. (2012) showing a 2-year record of wind work (top) and near-inertial kinetic energy (bottom) in the Northeast Pacific; b) one estimate of global power input (shading) and low-mode NIW energy fluxes (arrows; Simmons and Alford (2012)). c) Impact of near-inertial waves on annual mean precipitation in ocean climate models. The upper panel shows the mean precipitation (mm/day) from an experiment where the NI flux is set to 0.34 TW and the lower panel shows the same experiment but with a doubling of the NI flux to 0.68 TW. The total tropical precipitation in the two experiments differs by less than 1% An increase in near-inertial energy flux within observational uncertainties ameliorates the double ITCZs in the Atlantic and Pacific, and creates the South Pacific Convergence Zone; three significant improvements for climate simulations of tropical precipitation. . . . . 66

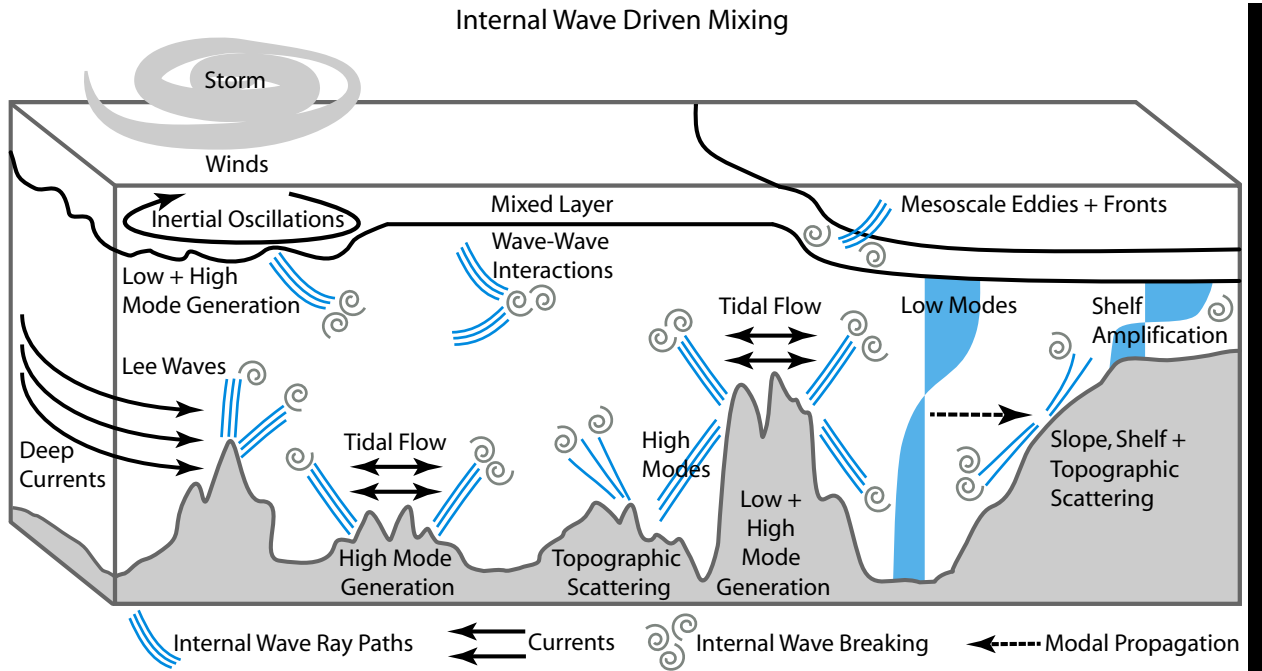


FIG. 1. Schematic of internal wave mixing processes in the open ocean that are considered as part of this CPT. Tides interact with topographic features to generate high-mode internal waves (e.g. at mid-ocean ridges) and low-mode internal waves (e.g. at tall steep ridges such as the Hawaiian Ridge). Deep currents flowing over topography can generate lee waves (e.g. in the Southern Ocean). Storms cause inertial oscillations in the mixed layer, which can generate both low and high mode internal waves (e.g. beneath storm tracks). In the open ocean these internal waves can scatter off of rough topography and potentially interact with mesoscale fronts and eddies, until they ultimately dissipate through wave-wave interactions. Internal waves that reach the shelf and slope can scatter, or amplify as propagate towards shallower water.

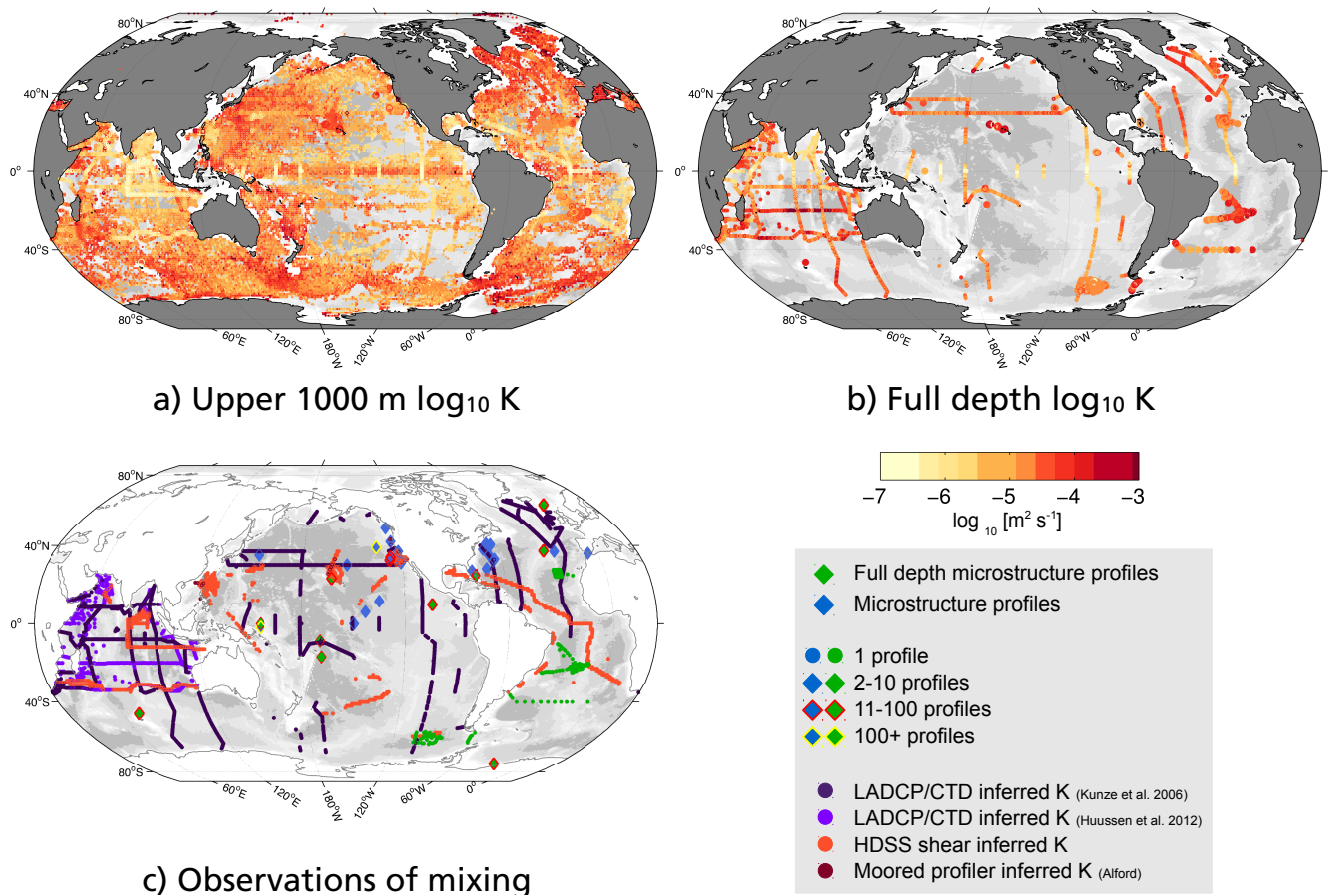


FIG. 2. Depth-averaged diffusivity  $\kappa$  from (a) the upper ocean (from MLD to 1000 m depth) and (b) the full water column, updated from (Waterhouse et al. 2014). The background diffusivity map in (a) comes from the strain-based inferences of diffusivity from Argo floats, updated from (Whalen et al. 2015) with observations included from 2006–2015. (c) Compiled observations of mixing measurements with blue and green squares and diamonds denoting microstructure measurements. Green represents full-depth profiles, while blue denotes microstructure profiles. Purple circles represent inferred diffusivity from a finescale parameterization using LADCP/CTD profiles [dark purple, Kunze et al. (2006); medium purple, Huussen et al. (2012)] and HDSS shipboard shear (light orange). Dark orange circles are diffusivities from density overturns in moored profiles.

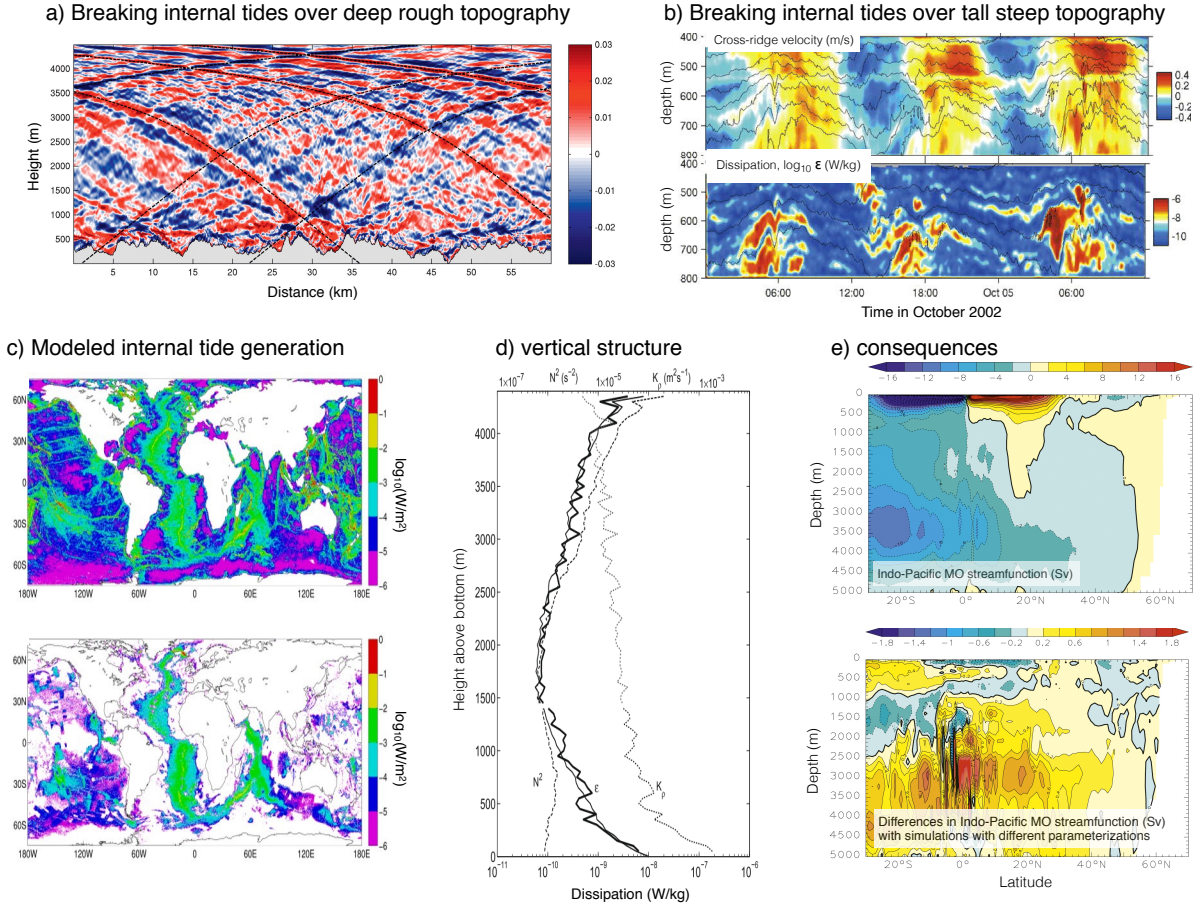


FIG. 3. a) A snapshot of baroclinic velocity (m/s) from a two-dimensional numerical simulation of internal tides forced by  $M_2$  (semi-diurnal) tidal velocities over rough topography, for parameters corresponding to the Brazil Basin (Nikurashin and Legg 2011); (b) observational time series of internal wave breaking over tall steep topography; here we see northward velocity (upper) and turbulent dissipation rate (lower) oscillate twice a day as the tide flows over Kaena Ridge, Hawaii (Klymak et al. 2008) (c) global energy flux from the  $M_2$  tide into internal tides (in  $\log_{10} W/m^2$ ) estimated using (top) the topography resolved in the SRTM30\_PLUS bathymetry data base and (bottom) a statistical representation of unresolved abyssal hill topography estimates (Melet et al. 2013b); (d) the vertical structure of dissipation from Brazil Basin observations (thick solid curve) and the Polzin 2009 (Eqn. 4) parameterization of nearfield internal tide dissipation (thin solid curve); (e) the impact of the Polzin parameterization in the GFDL CM2G coupled climate model: (top) The Indo-Pacific meridional overturning streamfunction (Sv)(averaged over the final 100 years of a 1000 year simulation) using the Polzin (2009) parameterization, (bottom) the differences in Indo-Pacific meridional overturning streamfunction (Sv) between the simulations with the Polzin (2009) parameterization and the St. Laurent et al. (2002) parameterization as implemented by Simmons et al. (2004b) (from Melet et al. (2013a)).



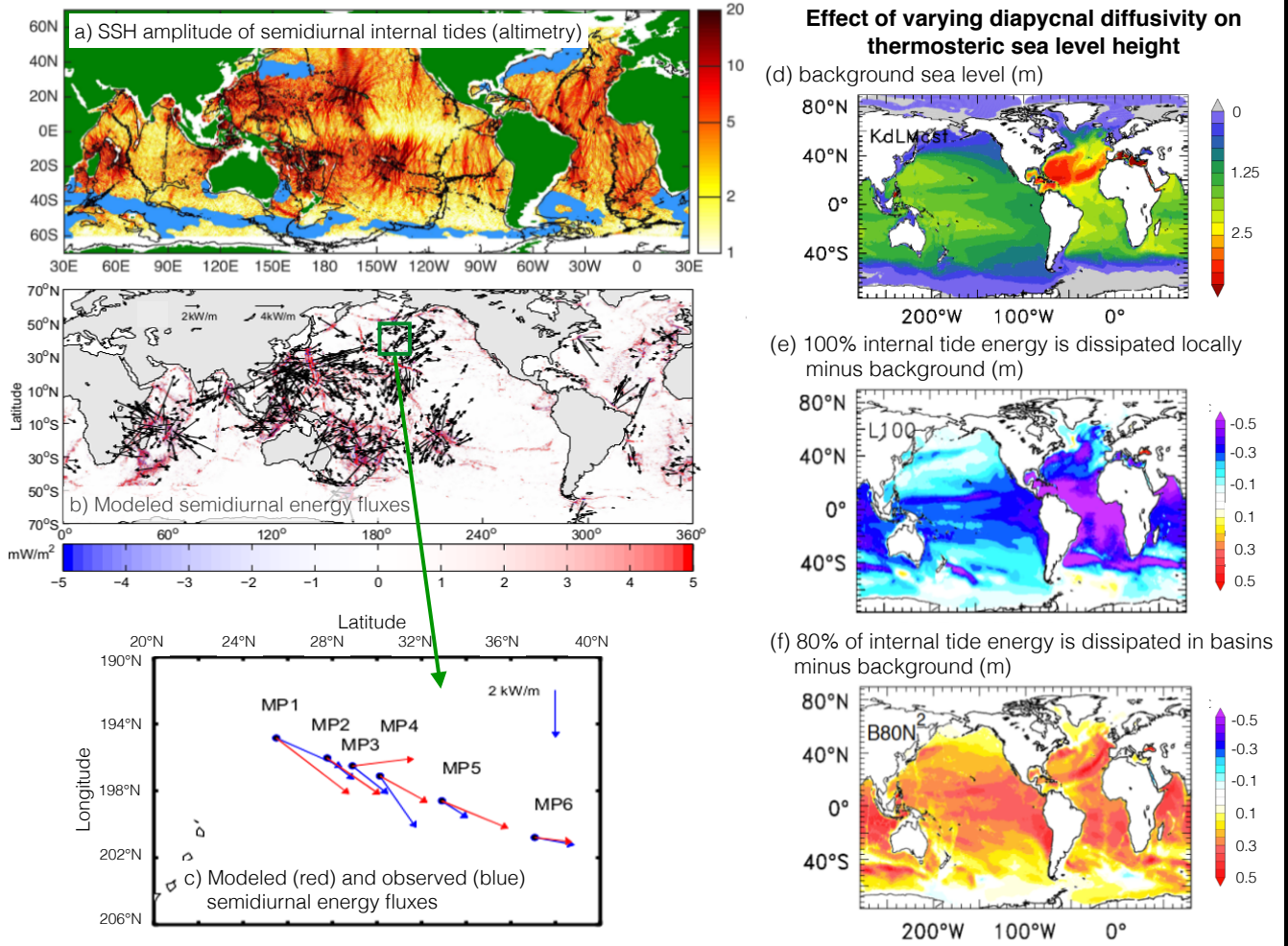
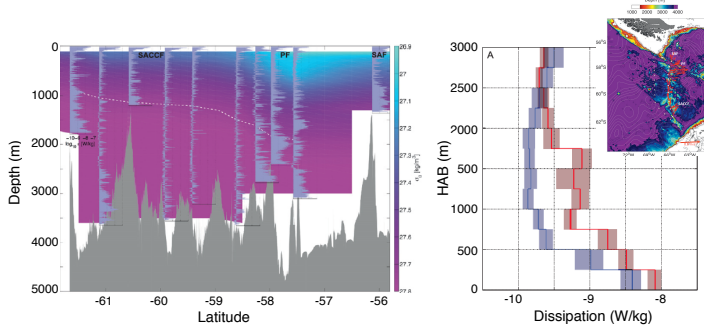
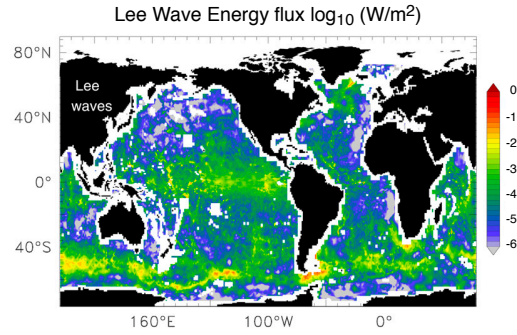


FIG. 4. Farfield internal tide: (a) SSH amplitude (unit: mm) of global mode-1  $M_2$  internal tides from multisatellite altimetry (Zhao et al. 2016). The light blue color indicates regions of high mesoscale activity, which make extraction of internal tides from altimetry difficult. (b)-(c) Modeled semidiurnal tidal fluxes and comparison to observations: (b) HYCOM modeled semidiurnal internal tide barotropic-to-baroclinic conversion rates (background color) and vertically-integrated energy flux vectors (black arrows, plotted every 768th grid point for clarity), and (c) depth-integrated semidiurnal mode-1 energy fluxes in HYCOM (red arrows) and high-resolution mooring observations to the north of Hawaii (blue arrows) (Ansong et al. 2017). (d)-(f) Impact on thermosteric sea level of using different spatial distribution of remote internal tide energy dissipation in GFDL ESM2G climate model: (d) thermosteric sea level (unit: m) in a reference simulation using a constant background diapycnal diffusivity for remote internal tide dissipation. Anomalies (in m) of thermosteric sea level from the reference case in (d) for simulations where (e) all internal tide energy is dissipated locally, over the generation site, (f) 20% of the internal tide energy is dissipated locally and 80% is dissipated uniformly over the ocean basins with a vertical profile proportional to buoyancy squared  $N^2$  (Melet et al. 2016).

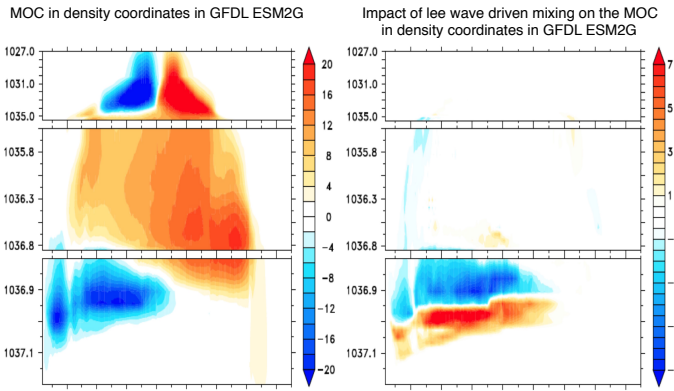
a) Lee waves: observations



b) power available: static parameterization



c) static parameterization: MOC impacts



d) power available: in-line parameterization

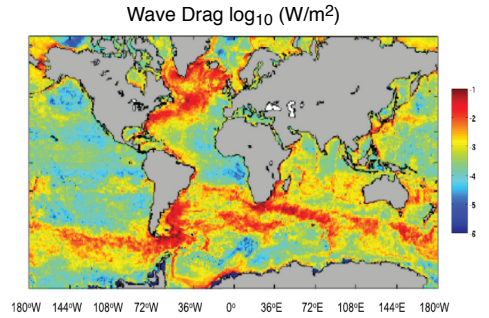
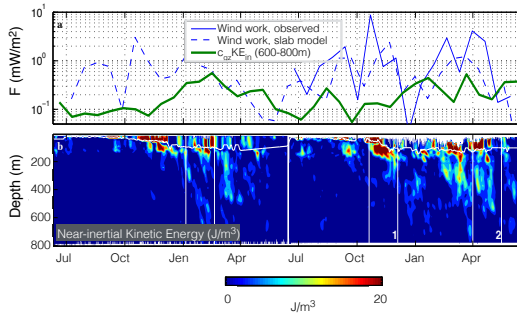


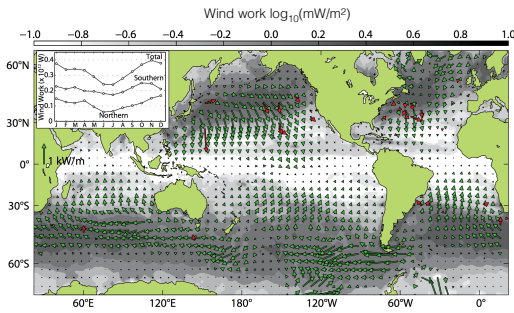
FIG. 5. Internal lee waves: a) observations from DIMES showing (left) turbulent dissipation rates (in logarithmic scales from  $10^{-10}$  to  $10^{-7}$   $\text{W kg}^{-1}$ ) for the Phoenix Ridge (circles in right inset), and (middle) average height above bottom profiles of turbulent kinetic energy dissipation (see details in St. Laurent et al. (2012)), b) power conversion into lee waves (Nikurashin and Ferrari (2011) used in Melet et al. (2014)), c) consequences of parameterized lee wave mixing on the global ocean meridional overturning circulation (Sv, averaged over the final 100 years of 1000 years simulations, from Melet et al. (2014)), d) global map of depth-integrated dissipation due to parameterized topographic wave drag inserted inline into global  $1/25^\circ$  HYCOM simulation, from Trossman et al. (2016).



### a) NIW: observational example



### b) NIW: global power input



### c) NIW: consequences

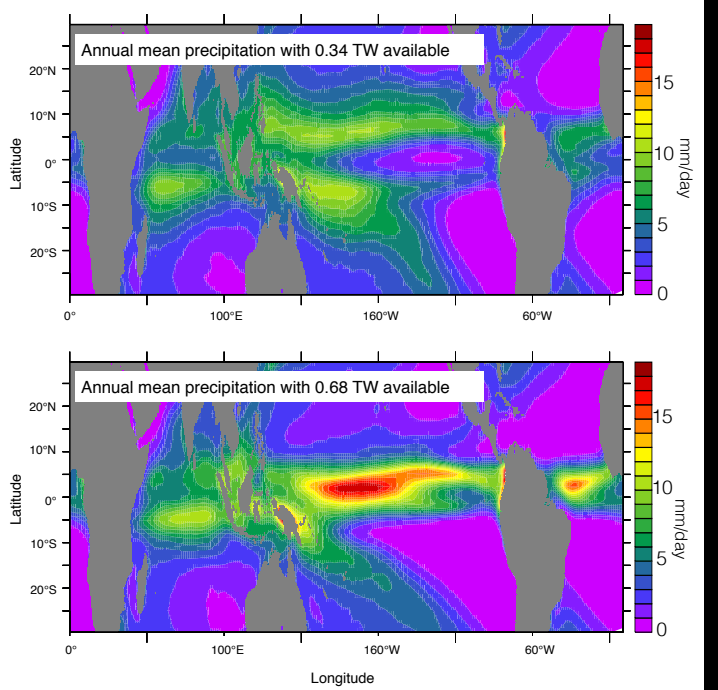


FIG. 6. Near-inertial internal waves: a) observational example from Alford et al. (2012) showing a 2-year record of wind work (top) and near-inertial kinetic energy (bottom) in the Northeast Pacific; b) one estimate of global power input (shading) and low-mode NIW energy fluxes (arrows; Simmons and Alford (2012)). c) Impact of near-inertial waves on annual mean precipitation in ocean climate models. The upper panel shows the mean precipitation (mm/day) from an experiment where the NI flux is set to 0.34 TW and the lower panel shows the same experiment but with a doubling of the NI flux to 0.68 TW. The total tropical precipitation in the two experiments differs by less than 1%. An increase in near-inertial energy flux within observational uncertainties ameliorates the double ITCZs in the Atlantic and Pacific, and creates the South Pacific Convergence Zone; three significant improvements for climate simulations of tropical precipitation.